The Astrophysical Journal, 1001:65 (21pp), 2026 April 10 https://doi.org/10.3847/1538-4357/ae4ecc

The Baryonic Mass–Halo Mass Relation of Extragalactic Systems

Stacy S. McGaugh[1], Tobias Mistele[1,2], Francis Duey[1], Konstantin Haubner[3,4], Federico Lelli[4], James M. Schombert[5], and Pengfei Li[6]
[1] Department of Astronomy, Case Western Reserve University, 10900, Euclid Avenue, Cleveland, OH 44106, USA
[2] Max Planck Institute for Extraterrestrial Physics, Giessenbachstrasse 1, 85748 Garching, Germany
[3] Dipartimento di Fisica e Astronomia, Universitá degli Studi di Firenze, via G. Sansone 1, 50019, Sesto Fiorentino, Firenze, Italy
[4] INAF—Arcetri Astrophysical Observatory, Largo Enrico Fermi 5, 50125 Firenze, Italy
[5] Institute for Fundamental Science, University of Oregon, Eugene, OR 97403, USA
[6] School of Astronomy and Space Science, Nanjing University, Nanjing, Jiangsu 210023, People's Republic of China
Received 2025 September 29; revised 2026 February 11; accepted 2026 March 6; published 2026 April 6

Abstract

We combine data for extragalactic systems to quantify a relation between the observed baryonic mass M_b and the enclosed dynamical mass M_{200} inferred from kinematics or gravitational lensing. Our sample covers 9 orders of magnitude in baryonic mass, including galaxies with kinematic or weak gravitational lensing data and groups and clusters of galaxies with new gravitational lensing data. For rich clusters with $M_b > 10^{14}\,M_\odot$, the observed baryon fraction is consistent with the cosmic value, $f_b = 0.157$. For lower masses, the baryon fraction decreases systematically with mass. The variation is well described by $M_b/M_{200} = f_b \tanh(M_b/M_0)^{1/4}$ with $M_0 \approx 5 \times 10^{13}\,M_\odot$. This relation is qualitatively similar to stellar mass–halo mass relations derived from abundance matching, but exhibits less scatter.

Unified Astronomy Thesaurus concepts: Galaxy clusters (584); Galaxy groups (597); Galaxy masses (607)

1. Introduction

There are a number of distinct missing mass problems in extragalactic astronomy. Most commonly, missing mass refers to the need for nonbaryonic cold dark matter (CDM; P. J. E. Peebles 1984; G. Steigman & M. S. Turner 1985) or a modification of the dynamical equations (e.g., M. Milgrom 1983a; C. Skordis & T. Złośnik 2021). There are also missing baryon problems, both globally for the whole Universe and locally in individual galaxies.

The global missing baryon problem is a shortfall in the inventory of observed baryons $\sum_i \Omega_i$ (e.g., M. Fukugita et al. 1998; J. M. Shull et al. 2012) relative to the expectation of Big Bang nucleosynthesis Ω_b (T. P. Walker et al. 1991; C. J. Copi et al. 1995). This long-standing problem now appears to be solved, with the bulk of the baryons residing in the intergalactic medium (IGM) so that $\sum_i \Omega_i \approx \Omega_b$ (L. Connor et al. 2025). However, the local missing baryon problem persists.

The local missing baryon problem is the shortfall in the mass of the observed stars and gas $M_b = M_* + M_g$ in any given object relative to the mass of baryons available in its dark matter halo, $f_b M_{200}$ ($f_b = \Omega_b/\Omega_m = 0.157$ is the cosmic baryon fraction; Planck Collaboration et al. 2020). Only the most-massive clusters of galaxies approach the limit $M_b \approx f_b M_{200}$ (e.g., A. H. Gonzalez et al. 2013; T. F. Laganá et al. 2013). Lower-mass systems have fewer detected baryons than their cosmic fair share, often by a large factor (S. S. McGaugh et al. 2010; H. Katz et al. 2018; L. Posti et al. 2019; K. B. W. McQuinn et al. 2022; A. Dev et al. 2024; P. E. Mancera Piña et al. 2025). In effect, there are two missing mass problems in most extragalactic systems: these local missing baryons and the presumptively nonbaryonic cosmic dark matter. This poses obvious questions: where are these unobserved baryons? What form do they take?

This paper focuses on quantifying the local missing baryon problem. We provide a new method to relate the enclosed dynamical mass M_{200} of extragalactic systems to their observed baryonic mass M_b. Our approach uses both kinematics and weak gravitational lensing to assess M_{200}, providing an estimate that is independent from abundance matching and the stellar mass–halo mass relations obtained therefrom (e.g., P. S. Behroozi et al. 2013; B. P. Moster et al. 2013; A. V. Kravtsov et al. 2018). These different approaches have some qualitative similarities but important quantitative differences.

In Section 2 we lay out the necessary conceptual framework, while Section 3 describes the data we utilize, including novel data for groups of galaxies. Section 4 gives our result in the form of a baryonic mass–halo mass relation. In Section 5, we compare this relation to stellar mass–halo mass relations from abundance matching, and discuss the implications of the variation of the baryon fraction with mass. Conclusions are given in Section 6.

The individual galaxies in our samples have direct distance determinations available in the Extragalactic Distance Database (R. B. Tully et al. 2009). This is not the case for the groups and clusters, for which we utilize Hubble flow distances (K. Haubner et al. 2025). For these to be on a consistent scale with galaxy data, we adopt $H_0 = 73\,\mathrm{km\,s^{-1}\,Mpc^{-1}}$ (A. G. Riess et al. 2022).

2. Galactic Mass Components

Galaxies reside at the centers of nonbaryonic dark matter halos. Their baryons exist in multiple components: stars, gas in various phases, and dust. The galaxies that we see are dominated by stars and cold (atomic and molecular) gas, typically within the central tens of kiloparsecs

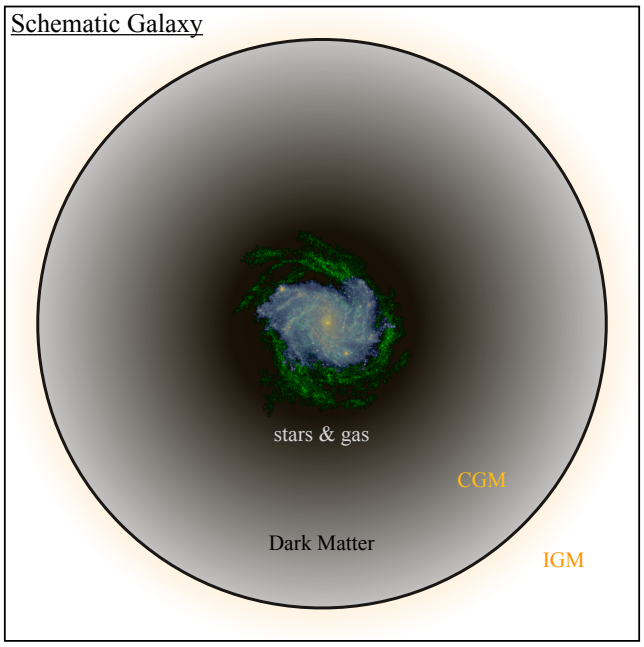

Figure 1. Conceptual elements of a galaxy: the stars (yellow/blue) and atomic gas (green) of NGC 6946 (Spitzer 3.6μ and 21 cm data: F. Walter et al. 2008) are shown embedded in an extended dark matter halo (black). The dark matter density decreases continuously with radius so the halo has no hard edge, but for convenience, we adopt the common convention that the radius r_{200} marks the boundary of the dark matter halo and the dividing line between the CGM and IGM (orange). The stars and gas illustrated here appear within $r < 20$ kpc while $r_{200} \approx 220$ kpc (not shown to scale).

(Z. Hua et al. 2025). Their dark matter halos extend much farther out, typically hundreds of kiloparsecs, as depicted schematically in Figure 1.

Beyond the confines of the visible galaxy, there may also be some baryons mixed in with the dark matter: the circumgalactic medium (CGM). We adopt the working definition that baryonic material within r_{200} not otherwise accounted for is part of the CGM while material beyond r_{200} is the IGM. We discuss each of these mass components below.

2.1. Stars

The defining content of galaxies is their stars. Stars dominate the baryonic mass of bright galaxies, and stellar mass is the key measurable quantity utilized by abundance matching relations. For the individual galaxies in our sample (Section 3), stellar masses are estimated from luminosities and colors using stellar population models (E. N. Taylor et al. 2011; J. Schombert et al. 2019, 2022). These have become both precise (S. S. McGaugh & J. M. Schombert 2014, 2015) and, for galaxies with direct distance measurements, reasonably accurate (F. Duey et al. 2025).

2.2. Interstellar Medium

The space between stars in galaxies contains dust and gas of various phases: molecular, atomic, and ionized. The dominant mass component in the ISM of most late-type galaxies is atomic gas, which is well traced by the 21 cm line of atomic hydrogen. The relation of gas mass to 21 cm luminosity follows from the physics of the spin-flip transition (B. T. Draine 2011), so gas masses can be both precise and accurate. We account for metallicity and molecular gas mass using scaling relations (S. S. McGaugh et al. 2020). Ionized gas is important in early-type galaxies, for which we also employ a scaling relation (see Appendix A). The mass of dust is negligibly small relative to the other components of the ISM.

2.3. Circumgalactic Medium

Coronal gas has been detected around some bright galaxies in various ways, including absorption lines of highly ionized oxygen (J. N. Bregman 2007; J. Tumlinson et al. 2017), X-ray emission (J.-T. Li et al. 2018; Y. Zhang et al. 2024a, 2024b, 2025), and the Sunyaev–Zel'dovich effect (C. T. Pratt et al. 2021; J. N. Bregman et al. 2022). These detections clearly show that there are baryons beyond the visible extent of galaxies. The mass in the CGM around L^* galaxies may be comparable to that in stars and other known baryons (J. N. Bregman et al. 2018), albeit with considerable uncertainty. Most of the CGM mass is inferred to reside at very large radii, so much depends on the extrapolation of power-law profiles and various other assumptions (Y. Zhang et al. 2025b).

Detections of the CGM are limited to bright galaxies ($M_* \gtrsim 10^{10}\,M_\odot$; S. Andreon et al. 2017; Y. Zhang et al. 2024b). There are many galaxies of lower mass in our sample for which the baryonic mass of the CGM is not constrained. In analogy with the intracluster medium in rich clusters of galaxies, it is tempting to imagine that the local missing baryonic mass is made up by the CGM. However, it is far from clear that this is viable for lower-mass galaxies (G. D. Bothun et al. 1994; A. Marasco et al. 2023).

2.4. Dark Matter Halo

The total extent and mass of dark matter halos remains a rather notional quantity. Kinematic measurements provide strong constraints on the enclosed mass:

$$M(<r) = rV^2/G \tag{1}$$

for spherical dark matter halos, but generally provide only lower limits as they do not reach the edge of the halo. Observationally, rotation curves become approximately flat at large radii, and persist in remaining flat as far out as measured. Weak gravitational lensing observations suggest that this behavior persists to Mpc scales (M. M. Brouwer et al. 2021; T. Mistele et al. 2024a). We utilize both kinematic and lensing data to make empirical estimates of the enclosed mass $M_{200}(r < r_{200})$.

Dark-matter-only structure formation simulations produce dark matter halos of the Navarro–Frenk–White (NFW) form (J. F. Navarro et al. 1997). This primordial initial condition can be altered by subsequent processes like adiabatic contraction (e.g., O. Y. Gnedin et al. 2004; J. A. Sellwood & S. S. McGaugh 2005; P. Li et al. 2022a, 2022b) and baryonic feedback (e.g., A. R. Duffy et al. 2010; F. Governato et al. 2012; A. Di Cintio et al. 2014a, 2014b; J. S. Bullock & M. Boylan-Kolchin 2017). Here, we are concerned only with the halo mass, for which we adopt the common convention of the mass M_{200} contained within the radius r_{200} enclosing an overdensity of 200 times the critical density of the Universe (Equation (10) of S. S. McGaugh 2012). This choice is somewhat arbitrary and is made to enable comparison with abundance matching relations; it is straightforward to adjust our results to other

choices of halo radius or overdensity (Equation (12) of S. S. McGaugh 2012).

The circular velocity V_{200} of a test particle at r_{200} is related to the enclosed mass by

$$M_{200} = B\, V_{200}^3. \quad (2)$$

For $H_0 = 73\,\mathrm{km\,s^{-1}\,Mpc^{-1}}$, $B = 3.3 \times 10^5\, M_\odot\,\mathrm{km^{-3}\,s^3}$ at $z = 0$ (M. Steinmetz & J. F. Navarro 1999). Note that because of the definition of the critical density, $V_{200} \propto r_{200}$, so Equations (1) and (2) are consistent. We will utilize kinematic (F. Lelli et al. 2019) and lensing measurements (T. Mistele et al. 2024a) of the flat rotation velocity, V_f, as an indicator of V_{200} and hence M_{200} via Equation (2).

2.5. Baryonic Mass Budget

The sum of the baryonic components discussed above sum to the baryonic mass of an extragalactic system, which we can compare to the expected mass of available baryons, $f_b M_{200}$. We have assembled a large sample of galaxies and systems of galaxies (Section 3) for which we have accurate measurements of the mass in stars and cold gas for each individual galaxy, and of the intracluster gas in rich clusters of galaxies. Conspicuously missing are accurate measurements of the CGM for individual galaxies. We therefore split the baryonic mass budget into two terms. The first is for the cold, condensed inner regions, i.e., the galaxies proper, for which

$$M_b = M_* + M_g. \quad (3)$$

This is well measured, but generally falls short of the expected total, $f_b M_{200}$. The second term is thus the missing baryons,

$$M_X = f_b M_{200} - M_b. \quad (4)$$

Some of these "missing" baryons may be in the CGM and not missing at all. However, some baryons may have been lost to the IGM, so we do not assume that $M_X = M_{CGM}$. Instead, we will obtain an expression for M_X given the accurately observed M_b and V_f, and discuss the prospects for these baryons to be part of the CGM or lost to the IGM.

It is common to discuss the stellar fraction

$$m_* = \frac{M_*}{M_{200}} \quad (5)$$

in the context of stellar mass–halo mass relations obtained from abundance matching (e.g., P. S. Behroozi et al. 2013; B. P. Moster et al. 2013; A. V. Kravtsov et al. 2018). This makes sense when attempting to reconcile the galaxy luminosity function with the halo mass function. However, all of the cold baryonic mass matters to the kinematics; the stellar mass alone is a poor proxy, especially for low-mass galaxies (S. S. McGaugh et al. 2000). We therefore consider the baryonic mass fraction, the ratio of observed baryons to the halo mass:

$$m_b = \frac{M_b}{M_{200}}. \quad (6)$$

The quantitative variation of m_b with mass is the primary result of this paper. We find a variation of m_b with mass that is robust, but its absolute normalization is contingent on the halo mass, which in turn depends on the relation between the circular velocity of the halo and that which is observed.

2.6. The Velocity Factor

We utilize measurements of the flat rotation velocity inferred from kinematics or gravitational lensing to estimate the dynamical mass M_{200} via Equation (2). This requires the velocity factor

$$f_v = \frac{V_f}{V_{200}}. \quad (7)$$

A circular speed curve that persists in remaining flat indefinitely corresponds to $f_v = 1$: the rotation speed at the virial radius is the same as that observed. The persistence of flat rotation curves to large radii led to the widespread assumption that this was indeed the case, with asymptotic flatness built into the pseudo-isothermal halo that was frequently used in mass modeling (e.g., Equations (1)–(3) of W. J. G. de Blok & S. S. McGaugh 1997). Empirically, there remains little evidence to contradict this assumption, and some to support its continuation remarkably far out (to ∼1 Mpc: T. Mistele et al. 2024a).

The velocity factor f_v cannot differ too much from unity and still explain the flatness of observed rotation curves, but slight differences are possible. For halos consistent with CDM simulations, the outer density profile is expected to fall off as $\rho \propto r^{-3}$, so the rotation curve should decline somewhat as it approaches the virial radius, implying f_v close to but slightly larger than unity. Figure 2 shows the observed V_f versus the fitted V_{200} for two-halo models, the pseudo-isoithermal (T. S. van Albada et al. 1985; W. J. G. de Blok & S. S. McGaugh 1997; J. Kormendy & K. C. Freeman 2016) and NFW (J. F. Navarro et al. 1997) halos. We use the fits[7] of P. Li et al. (2020) that have not been constrained with ΛCDM priors to illustrate what the data alone can tell us. As expected, the projected value of V_{200} for the pseudo-isothermal model closely tracks the observed flat velocity, corresponding to $f_v = 1$. For the NFW model, the better data are offset from the one-to-one line by $f_v \approx 1.4$ (see also H. Katz et al. 2019; L. Posti et al. 2019). This goes in the expected direction ($V_f > V_{200}$ since rotation curves should decline), but there is an enormous amount of scatter in the value of f_v inferred.

The scatter seen in Figure 2 for the NFW model happens for a number of reasons. For one, it is difficult to constrain the rotation speed at the virial radius with rotation curves that do not extend that far out. Consequently, only the most extended rotation curves provide interesting constraints. More generally, NFW halos do not typically provide a good description of the data (S. S. McGaugh et al. 2007; H. Katz et al. 2017). One symptom of the cusp-core problem is a propensity for fits to exaggerate the overall size of a halo to compensate for the mismatch in shape at small radii (W. J. G. de Blok et al. 2001). An example of this is provided by the galaxies in Figure 2 with $V_f \approx 60\,\mathrm{km\,s^{-1}}$ but $V_{200} \approx 300\,\mathrm{km\,s^{-1}}$. These dwarf galaxies, with $M_b \approx 6 \times 10^8\, M_\odot$, presumably do not reside in dark matter halos with masses $M_{200} \approx 10^{13}\, M_\odot$ that would outweigh the entire Local Group. Clearly we need to exercise caution in attempting to infer the value of f_v, which may also differ for different halo models (P. Li et al. 2020).

Despite these difficulties, it is important to note that there is very little scatter in the Tully–Fisher relation (R. B. Tully & J. R. Fisher 1977), especially when V_f is used as the rotation

[7] Note that V_{200} of the fitted model is a parameter of the dark matter halo alone, so is subtly different from M_{200} as defined here to include baryons.

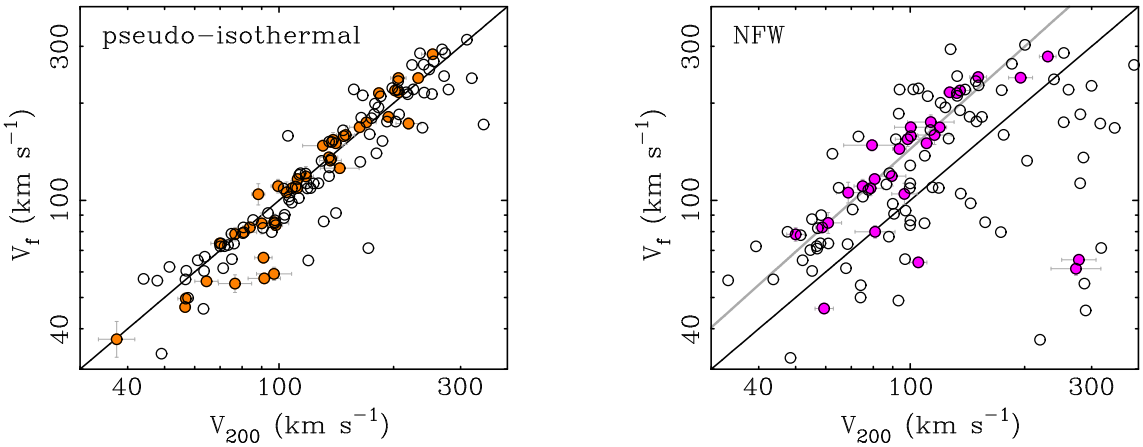

Figure 2. The observed flat velocity V_f as it relates to the fitted V_{200} for pseudo-isothermal (left panel) and NFW (right panel) halos (P. Li et al. 2020). Filled points have formal uncertainties <20% in V_{200}; open points are less accurate fits. The solid line shows $V_f = V_{200}$. The gray line in the right panel shows Equation (2a) of H. Katz et al. (2019), which corresponds roughly to $f_v \approx 1.4$.

speed measure (F. Lelli et al. 2019). We will accept this as a sign that the observed flat rotation speed is indeed closely related the halo mass, as often assumed. We thus adopt $f_v = 1$ for illustration, and will explore variations in this parameter in Section 5.

2.7. Constraints from Tully–Fisher

For rotationally supported galaxies, M_b and V_f are tightly correlated through the Baryonic Tully–Fisher Relation (BTFR):

$$M_b = A\, V_f^4 \tag{8}$$

with $A = 50\, M_\odot\, \mathrm{km}^{-4}\, \mathrm{s}^4$ (S. S. McGaugh 2005). The best fit has consistently been in the range $1.65 \leqslant \log A \leqslant 1.75$ for 20 yr (S. S. McGaugh 2012; F. Duey et al. 2026, in preparation). Some of this variation is from fitting uncertainty, and some is from differences in stellar population models and correction factors for metallicity and molecular gas (S. S. McGaugh et al. 2020).

The observed slope of the BTFR is indistinguishable from 4 (S. S. McGaugh & J. M. Schombert 2015; J. Schombert et al. 2020; F. Duey et al. 2026 in preparation). This is steeper than the slope 3 of the theoretical halo mass–circular velocity relation (Equation (2)). This difference requires a systematic variation of m_b or f_v or both with mass. The simplest way to reconcile the expected $M_{200} \propto V_{200}^3$ with the observed $M_b \propto V_f^4$ is for m_b to increase linearly with V_f (S. S. McGaugh 2012). More generally, some combination of variation of both m_b and f_v is possible, but in practice, it is difficult to explain much of the required variation with the velocity factor f_v (Figure 2). Consequently, one inevitably infers a strong variation of the baryon fraction m_b with mass.

Combining the equations above to transform the BTFR into the baryonic mass–halo mass plane, we have

$$m_b = \frac{A}{B} f_v^3\, V_f, \tag{9}$$

which is the linear dependence on V_f with allowance for variation in f_v. Since the baryonic mass is generally more accessible observationally than the flat rotation speed, we can also write

$$m_b = \frac{A^{3/4}}{B} f_v^3\, M_b^{1/4} \tag{10}$$

(see also Equations (16) and (17) of S. S. McGaugh 2012, where the detected baryon fraction $f_d = m_b/f_b$).

These simple relations hold only for rotationally supported galaxies. Below we generalize this result to other types of systems over nine decades in baryonic mass.

3. Data

We measure the baryon fraction in galaxies from dwarfs with $M_b \approx 10^6\, M_\odot$ to giants with $M_b \approx 4 \times 10^{11}\, M_\odot$ continuing through groups of galaxies to rich clusters up to $M_b \approx 5 \times 10^{14}\, M_\odot$. The lensing mass estimates for groups are the novel contribution of this work. Data for other systems are taken from other papers, as discussed below. We make no adjustments to published results except to reconcile all data to the same distance scale ($H_0 = 73\, \mathrm{km\, s^{-1}\, Mpc^{-1}}$).

There exist accurate data for the stellar and gas masses for many galaxies. We take the baryonic mass of each object to be the sum of measured stars and gas (Equation (3)), as discussed in the papers describing the data. Measurements for the mass of the coronal gas in the CGM are not available for the vast majority of objects with otherwise excellent data, so we do not include it in the sum. Instead, we obtain a relation between the measured baryonic mass $M_b = M_* + M_g$ and corresponding baryon fraction $m_b = M_b/M_{200}$. This can be used to infer how much mass M_X is missing, which in turn provides a constraint on the mass in the CGM, $M_{\rm CGM}$.

To estimate the dynamical mass M_{200} including dark matter, we utilize Equation (2) and measurements of the flat rotation velocity V_f. The flat rotation speed is estimated from either kinematic or gravitational lensing data. We take care to define an equivalent to the flat circular speed for pressure supported systems so that all objects are on a comparable scale.

3.1. Kinematic Data

3.1.1. Rotationally Supported Galaxies

WISE-SPARC Sample. These are spiral and irregular galaxies (F. Lelli et al. 2016a) with direct distance determinations

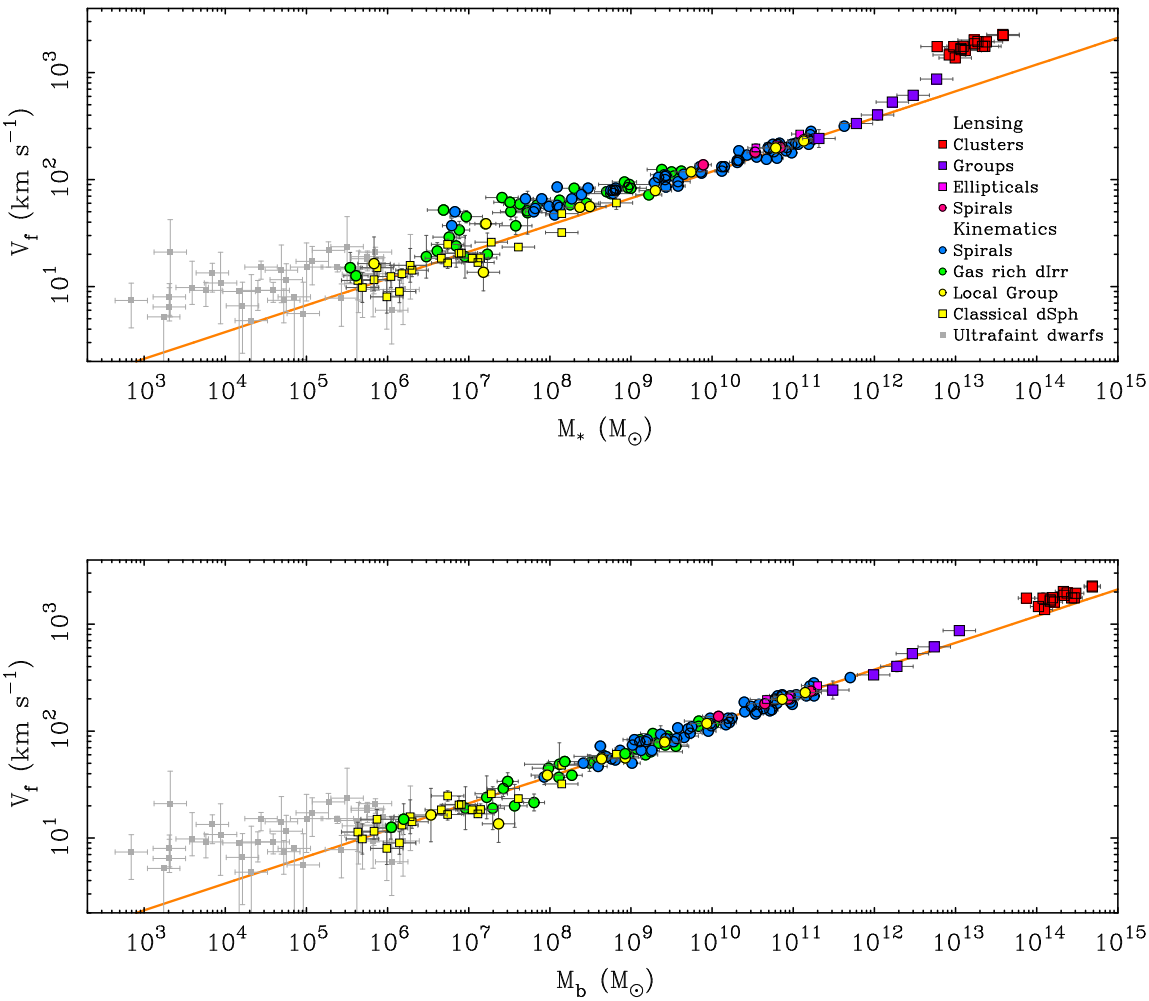

Figure 3. The flat-equivalent circular velocity of extragalactic systems as a function of stellar mass (top panel) and baryonic mass (bottom panel). Data for rotationally supported galaxies are depicted by circles; squares represent pressure supported systems. The blue circles are galaxies with directly measured distances, V_f from rotation curves, and stellar masses from WISE photometry from F. Duey et al. (2026, in preparation). Green circles are gas-rich galaxies ($M_g > M_*$; D. V. Stark et al. 2009; C. Trachternach et al. 2009; E. Z. Bernstein-Cooper et al. 2014; A. T. McNichols et al. 2016; G. Iorio et al. 2017; B. Namumba et al. 2025; J.-L. Xu et al. 2025) not in F. Duey et al. (2026, in preparation). Yellow points are Local Group galaxies, both spirals and dwarfs (S. S. McGaugh et al. 2021); gray squares are ultrafaint dwarfs (F. Lelli et al. 2017). Lensing results for early- and late-type galaxies (T. Mistele et al. 2024a) are shown as pink squares and magenta circles, respectively. Red squares are clusters of galaxies (T. Mistele et al. 2025), and purple squares are groups of galaxies (this work). The orange line is the BTFR (Equation (8)).

(F. Duey et al. 2026, in preparation) and stellar mass estimates based on Wide-field Infrared Survey Explorer (WISE) near-infrared photometry (F. Duey et al. 2024) and detailed stellar population models (F. Duey et al. 2025). The gas mass is calculated using the observed atomic gas mass and a scaling relation to account for the molecular gas content and the trend of metallicity with mass (S. S. McGaugh et al. 2020). Flat rotation speeds (F. Lelli et al. 2019) are measured from resolved 21 cm rotation curves using the algorithm of F. Lelli et al. (2016b).

Gas-rich Galaxy Sample. These are low-mass dwarf irregular galaxies that are not already in the WISE sample of F. Duey et al. (2024). These galaxies are dominated by atomic gas, with $M_g > M_*$, making the contribution of stars to the baryonic mass error budget small (S. S. McGaugh 2011). The data come from a variety of sources (D. V. Stark et al. 2009; C. Trachternach et al. 2009; E. Z. Bernstein-Cooper et al. 2014; A. T. McNichols et al. 2016; G. Iorio et al. 2017; B. Namumba et al. 2025; J.-L. Xu et al. 2025).

There is considerable overlap in mass between these gas-rich dwarf irregulars and the gas-poor dwarf spheroidals of the Local Group. The lowest-mass examples, Leo P (R. Giovanelli et al. 2013; E. Z. Bernstein-Cooper et al. 2014) and KK153 (J.-L. Xu et al. 2025), have circular velocities $V_f \approx 15\,\mathrm{km\,s^{-1}}$ and stellar masses $M_* \approx 4 \times 10^5\,M_\odot$ that are nearly in the ultrafaint regime. This places them well below the nominal threshold for quenching from reionization (K. B. W. McQuinn et al. 2015), which had been anticipated to be $\sim$40 $\mathrm{km\,s^{-1}}$ (R. A. Crain et al. 2007; M. Hoeft & S. Gottloeber 2010). Nevertheless, they exist, and are forming stars in disks dominated by cold gas.

Local Group Rotators. Galaxies range from M31 and the Milky Way at the high-mass end to DDO 210 and DDO 216 at the low-mass end. The latter two both have $V_f \approx 15\,\mathrm{km\,s^{-1}}$, making them comparable to the lowest-mass galaxies in the gas-rich sample, albeit with large uncertainties. The uncertainties are small for the more-massive members of the Local Group, which is reflected in their small scatter in Figure 3. The data are adopted from Table 1 of S. S. McGaugh et al. (2021).

3.1.2. Pressure Supported Local Group Dwarfs

Classical Dwarfs. These form a sequence in luminosity and velocity dispersion that parallels the BTFR (S. S. McGaugh et al. 2021). We adopt the data from Table 2 of that paper here. For

these galaxies, the two sequences are coincident when the factor $\beta = 2$ in $V_f = \beta\sigma$ assuming an average V-band mass-to-light ratio of $2\,M_\odot/L_\odot$. This value of β is only slightly larger than the nominal $\beta = \sqrt{3}$ expected for isotropic orbits, and may follow from the fact that V_f is typically measured at larger radii than σ (see the discussion in S. S. McGaugh et al. 2021).

Ultrafaint Dwarfs. With $L_V < 10^5\,L_\odot$ (J. D. Simon 2019), they do not parallel the BTFR as classical dwarfs do (F. Lelli et al. 2017). To a crude approximation, a tolerable depiction of the trend in the data is a constant $V_f \approx 10\,\mathrm{km\,s^{-1}}$ for $M_b < 5 \times 10^5\,M_\odot$. Allowing for a slope, the M_b–V_f relation obtained by S. S. McGaugh et al. (2010) for $V_f < 20\,\mathrm{km\,s^{-1}}$ remains consistent with the data despite many newly discovered dwarfs in the intervening time.

These ultrafaint dwarfs are all deep in the potential of the Milky Way where they are subject to considerable tidal perturbation. It therefore seems unlikely that their measured velocity dispersions are faithful indicators of their dynamical mass (S. S. McGaugh & J. Wolf 2010), so we will restrict our attention to more-massive systems. Historically, it is worth noting that the point at which galaxies appear to deviate from the BTFR has decreased from $V_f \approx 50\,\mathrm{km\,s^{-1}}$ (S. S. McGaugh 2005) to $\approx$20 $\mathrm{km\,s^{-1}}$ (S. S. McGaugh et al. 2010) to $\approx$10 $\mathrm{km\,s^{-1}}$ (now). This trend stems largely from improvements in data quality, so it is possible that it will continue as the data continue to improve. There is a clear distinction between a plateau of $\sim$10 $\mathrm{km\,s^{-1}}$ for the lowest-mass galaxies and the continued decrease predicted by the extrapolation of the BTFR. This can hopefully be tested with the discovery of isolated low-mass galaxies far from tidal influences that should be enabled by the Rubin Observatory and Square Kilometer Array.

3.2. Lensing Data

The equivalent of the flat circular velocity can be inferred from weak gravitational lensing observations with the method described by T. Mistele et al. (2024b). T. Mistele et al. (2024a) applied this method to the stacked data for large numbers of individual galaxies. T. Mistele & A. Durakovic (2024) extended the method to apply to individual clusters of galaxies (T. Mistele et al. 2025). Here, we apply it on the group scale.

3.2.1. Galaxies

Late-type Galaxies. These are adopted from the analysis of the KiDS-bright sample (M. Bilicki et al. 2021) by T. Mistele et al. (2024a). Late-type galaxies are defined as having $u - r < 2.5$ and are split into four bins by baryonic mass with thousands of galaxies per bin. The flat circular velocity is obtained by averaging the circular velocities at radii from $50 < r < 300$ kpc.

Early-type Galaxies. These are also adopted from T. Mistele et al. (2024a), taken there to be those galaxies with $u - r > 2.5$. They are analyzed in the same way as the late-type galaxies. The baryonic mass includes a correction for hot gas based on a scaling relation with stellar mass (see Appendix A). There are only three baryonic mass bins due to the small number of early-type galaxies in the lowest-mass bin.

Table 1
Weak Lensing Group Masses

Bin	N^a	z	V_f ($\mathrm{km\,s^{-1}}$)	M_b	M_* ($10^{12}\,M_\odot$)	M_*^{BCG}
1	521	0.1168	242 ± 47	0.307	0.207	0.084
2	769	0.1732	335 ± 31	0.978	0.601	0.188
3	295	0.2124	402 ± 46	1.894	1.095	0.283
4	456	0.2452	530 ± 30	2.942	1.666	0.337
5	398	0.2878	614 ± 33	5.461	3.001	0.406
6	206	0.3239	871 ± 42	11.164	5.851	0.540

Note.
[a] The number of groups informing the average quantities for each bin.

3.2.2. Galaxy Systems

Clusters of Galaxies. T. Mistele et al. (2025) obtained the flat circular velocity for 16 CLASH clusters from gravitational lensing data by averaging the implied circular velocities over radii between 750 kpc $< r <$ 3 Mpc. The baryonic masses are evaluated by integrating the beta profile fits of the hot gas to $r = r_{200}$. This is an extrapolation beyond the limits of direct observation. It integrates to a large mass that results in a reasonable baryon fraction, where other plausible extrapolations do not. To account for the stellar mass in cluster galaxies, T. Mistele et al. (2025) assumed $M_* = 0.08\,M_b$ following B. Famaey et al. (2025). More elaborate scaling relations (e.g., T. F. Laganá et al. 2013) do not change the basic result. It would obviously be preferable to directly measure the stellar mass of each cluster, but such data are not readily available. The uncertainty in the stellar mass is much smaller than that in the gas mass obtained from the extrapolation of the beta profile. Our results for clusters are in excellent agreement with ΛCDM, so it would become a problem if either our stellar or gas mass estimates were grossly in error. This also applies to dynamical masses, for which less favorable M_{200} can reasonably be inferred (P. Li et al. 2023).

Groups of Galaxies. We measure the stacked mass profiles of galaxy groups from GAMA-II (S. P. Driver et al. 2011; J. Liske et al. 2015) using KiDS-DR4 weak-lensing data (K. Kuijken et al. 2019; A. H. Wright et al. 2020; B. Giblin et al. 2021; H. Hildebrandt et al. 2021). Following previous works, we select groups with at least five members (e.g., M. Viola et al. 2015; D. Rana et al. 2022; S.-S. Li et al. 2024; Z. Liu et al. 2024) and split the data into bins by baryonic mass. For each M_b bin, we calculate averaged stellar and baryonic masses by summing up the respective quantities of the member galaxies and averaging over the groups in each bin. We obtain a stacked halo mass profile $M(r)$ using the nonparametric weak-lensing deprojection method from T. Mistele et al. (2024b) and T. Mistele & A. Durakovic (2024). We correct for miscentering and contributions from the two-halo term. These corrections are somewhat uncertain, but have only a moderate effect in the radial range we consider. We convert $M(r)$ into a circular velocity profile $V_c(r) \equiv \sqrt{GM(r)/r}$ and take V_f to be the weighted average of the circular velocities at radii between 800 kpc and 2 Mpc. The results are provided in Table 1 with details explained in Appendix A.

4. Results

The data described above are shown together in Figure 3. There is a strong correlation between the flat rotation speed

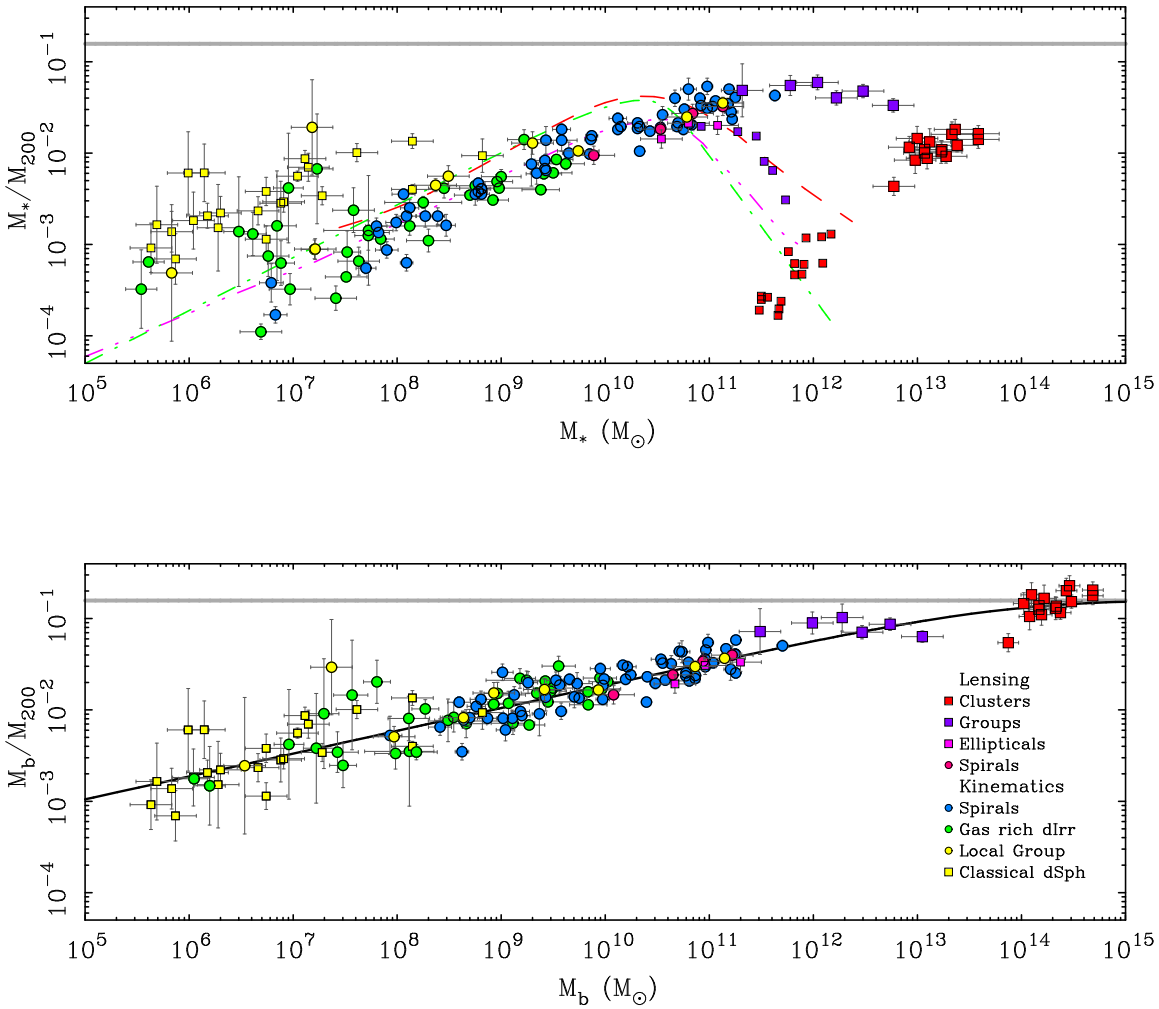

Figure 4. The stellar mass fraction as a function of stellar mass (top) and the baryonic mass fraction as a function of baryonic mass (bottom). Data and symbols as in Figure 3 with the additional distinction that large squares in the top panel represent the sum of the stellar mass of all galaxies in a group or cluster while small squares are the stellar mass of the brightest galaxy only. The horizontal line is the cosmic baryon fraction $f_b = 0.157$ (Planck Collaboration et al. 2020). The colored lines in the top panels show the stellar mass–halo mass relations from abundance matching given by B. P. Moster et al. (2013; dashed–dotted green line), P. S. Behroozi et al. (2013; dashed–triple dotted pink line), and A. V. Kravtsov et al. (2018; red dashed line). The black line in the lower panel is Equation (12).

and both stellar mass and baryonic mass. These relations are analogous to the Tully–Fisher relation, but including extragalactic systems from ultrafaint dwarfs to rich clusters of galaxies.

The stellar fraction $m_* = M_*/M_{200}$ and the measured baryon fraction $m_b = M_b/M_{200}$ are shown in Figure 4. The halo mass is computed using V_f in Equation (2) with $f_v = 1$. Some of the groups and clusters are at modest redshift, so we account for the expected evolution of the intercept in the M_{200}–V_{200} relation (J. C. Muñoz-Cuartas et al. 2011). For the range of observed redshifts, this can be tolerably approximated as $\log B(z) = 5.508 - 0.256z$. For the highest-redshift cluster (MACSJ0744 at $z = 0.686$), this is a 0.18 dex correction. Though modest, this is important to getting the baryon fraction right.

4.1. Kinematic Mass Matching Relation

Mathematically, the measured baryon fraction is well described by embedding the BTFR (Equation (8)) within a hyperbolic tangent that transitions from the monotonic rise of m_b on galaxy scales to a constant value at high mass. Specifically,

$$m_b = f_b \tanh\left(\frac{V_f}{V_0}\right) \tag{11}$$

$$= f_b \tanh\left(\frac{M_b}{M_0}\right)^{1/4} \tag{12}$$

where we have obliged the function to asymptote to the cosmic value $f_b = 0.157$ at high mass. It need not have been the case that the asymptotic value would agree so well with the cosmic value, but it does, at least for our choice of M_{200} for the halo mass and the extrapolation of the β-profile of the X-ray gas. The turnover region is not well sampled by data, so the precise value of the parameter M_0 is not well constrained. Equation (12) is illustrated in Figure 4 with $\log(M_0/M_\odot) = 13.7$, which is equivalent to $V_0 = 1000\,\mathrm{km\,s^{-1}}$ in Equation (11).

Equation (12) works well for objects with $M_b > 5 \times 10^5\,M_\odot$ irrespective of whether they are individual galaxies or galaxy systems. It does not matter whether a galaxy system is a group or a cluster, nor whether an individual galaxy has its baryonic

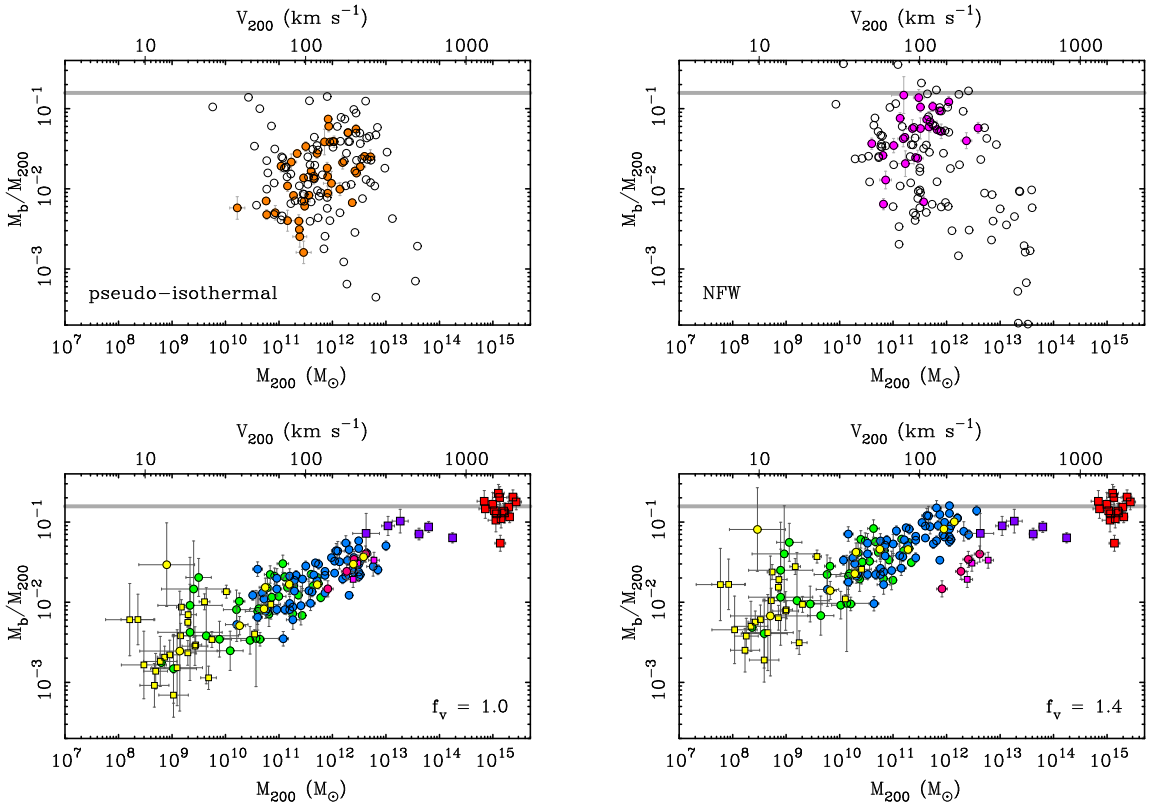

Figure 5. The baryonic mass fraction as a function of mass M_{200} with the equivalent V_{200} noted on the top axis. Data and symbols are the same as in Figures 2 and 3. The top panels follow from using rotation curve fits to estimate halo mass as in Figure 2 for pseudo-isothermal (top-left panel) and NFW (top-right panel) halo models. The bottom panels follow from using the flat rotation speed as the halo mass estimator as in Figure 3 with $f_v = 1.0$ (bottom-left panel) or $f_v = 1.4$ (bottom-right panel) for the kinematic data; the lensing data are unchanged.

mass dominated by stars or gas. The data fall along the same relation with remarkably little scatter.

We can find no indication of second-parameter dependences: the baryon fraction depends only on mass. It does not depend on the star formation history, as both red and dead galaxies have the same baryon fraction as active star formers of the same mass, contrary to what is seen in some simulations (e.g., Figure 5 of J. Oñorbe et al. 2015). This would seem to contradict feedback from star formation as the driving reason for the variation in baryon fraction. Neither does the environment seem to play a role, as there is no segregation in circular velocity between star-dominated satellite galaxies and isolated gas-rich galaxies of the same baryonic mass (Figure 3). It is difficult to find a satisfactory explanation for all aspects of the observations: the systematic variation with mass, the small scatter, and the apparent absence of second-parameter effects.

4.2. Variations in Approach

We have used the flat circular velocity to obtain the enclosed dynamical mass above, assuming $V_{200} = V_f$. Other approaches are possible. In Figure 5 we illustrate the results if we make use of full rotation curve fits or different assumptions about the factor f_v relating V_f to V_{200}.

The top panels of Figure 5 show the baryon fraction using results of fitting halo models to rotation curves (P. Li et al. 2020). As expected, the large scatter in Figure 2 translates into large scatter in Figure 5. A trend of the baryon fraction with mass is perceptible, but only barely. The large scatter is an artifact of the procedure: halo masses M_{200} are not well constrained by detailed fits where the halo parameters are degenerate with the mass-to-light ratio of the stars and with nuisance parameters like distance and inclination. For the NFW case (top-right panel), the baryon fraction sometimes reaches the cosmic value, so we corroborate the result of P. E. Mancera Piña et al. (2025) in this regard, but note that this result depends on the specific halo choice and fitting procedure (H. Katz et al. 2017; P. Li et al. 2020). We do not concur with their interpretation that this explains the so-called diversity of rotation curves, as the scatter here is an artifact.

The bottom panels use V_f as the halo mass indicator. The flat rotation speed has long been assumed to be the signature of the dark matter halo; the reduction in scatter going from the top panels of Figure 5 to the bottom panels seems to bear that out. The bottom-left panel assumes $f_v = 1$, so is identical to the bottom panel of Figure 4 except for the abscissa showing halo properties rather than baryonic mass. Since we adopt $V_{200} = V_f$ here, by construction, these data are well described by Equation (11).

The bottom-right panel of Figure 5 adopts $f_v = 1.4$ for galaxies with kinematic data as suggested in Figure 2. This provides a scale consistent with NFW halo fits (H. Katz et al. 2017; P. Li et al. 2020) without incurring the penalty of the scatter therein. The data shift up relative to the bottom-left panel because $f_v > 1$ corresponds to a smaller dynamical mass than $f_v = 1$, so the baryon fraction $m_b = M_b/M_{200}$ goes up. As in the top-right panel, a few galaxies reach the cosmic value, though most do not. The turnover scale is lower, $\log(M_0/M_\odot) \approx 11.6$, but the asymptote to the cosmic baryon fraction is less clear.

The factor f_v is present to relate the flat rotation speed observed in kinematic data at typical radii of tens of kiloparsecs with virial radii of hundreds of kiloparsecs. This does not apply to the lensing data, which themselves sample hundreds of kiloparsecs out (T. Mistele et al. 2024a). We therefore leave $f_v = 1$ for the lensing data in the bottom-right panel of Figure 5. This creates an artificial tension with the kinematic data that can be seen as an offset in the points with $M_{200} \approx 10^{12}\,M_\odot$. That this offset appears as an artifact of the choice of f_v implies that $f_v \approx 1$ is preferred.

5. Discussion

5.1. Comparison with Abundance Matching

Equation (12) provides a relation between the observed baryonic mass and the halo mass indicated by kinematics and gravitational lensing. A similar mapping between the visible and invisible is provided by stellar mass by way of abundance matching (e.g., P. S. Behroozi et al. 2013; B. P. Moster et al. 2013; A. V. Kravtsov et al. 2018). We compare[8] the two here.

There is reasonable agreement between the kinematic mass indicated by V_f and the stellar mass–halo mass relations from abundance matching over the range $7.7 \lesssim M_* \lesssim 10.7\,M_\odot$. The modest offset between the kinematic data and any one of the illustrated abundance matching relations can be trivially reconciled with a judicious choice of the velocity factor f_v (L. Posti et al. 2019). However, the apparent agreement does not hold outside this mass range.

At high masses ($M_* > 10^{11}\,M_\odot$), the abundance matching relations diverge from the kinematic data. This is partly due to a difference in definitions. For the stellar mass, we include all the stars in all the galaxies in a group or cluster. In contrast, abundance matching references the stellar mass of the brightest cluster galaxy (BCG) alone, with the notional identification of the BCG[9] with the "central" galaxy of the entire cluster halo, the other cluster galaxies being satellites residing in subhalos. However, Figure 4 shows that for larger masses, the stellar mass of an individual galaxy is not a good indicator of the halo mass. At $M_* \approx 4 \times 10^{11}\,M_\odot$, a galaxy could be the central of a large cluster, a modest group, or be isolated. The corresponding stellar fraction m_* ranges over 2 orders of magnitude from $m_* \approx 2 \times 10^{-4}$ for the central of a rich cluster with $M_{200} \approx 2 \times 10^{15}\,M_\odot$ to $m_* \approx 3 \times 10^{-3}$ for a galaxy that is the central of a group with $M_{200} \approx 10^{14}\,M_\odot$ to $m_* \approx 0.04$ for an isolated spiral with $M_{200} \approx 10^{13}\,M_\odot$. Simply looking at the stellar mass of each of these galaxies does not suffice to indicate the halo mass. Even around $M_* = 10^{11}\,M_\odot$ there is a large offset between the kinematically indicated mass and that expected from abundance matching (S. S. McGaugh & P. van Dokkum 2021).

At low masses ($M_* < 10^{7.5}\,M_\odot$), there is a bifurcation of m_* between star-dominated and gas-dominated galaxies. The stellar fraction of the gas-poor, early-type dwarfs of the Local Group differs from that of gas-rich star-forming dwarfs by a large factor at the same stellar mass. The latter are in approximate agreement with abundance matching relations based on field galaxy luminosity functions. However, application of such abundance matching relations to the classical dwarfs of the Local Group will result in halo mass estimates differing from the kinematic value by an order of magnitude.

The bifurcation seen in m_* between star-dominated and gas-dominated galaxies does not occur for m_b. Whatever physics drives this relation, it depends on the mass of baryons in galaxies, not whether those baryons are in the form of stars or gas. Neither does it depend on the details of the star formation history of each galaxy, as one might expect if feedback is the physics that determines m_b. Galaxies that formed their stars long ago and contain no gas now have the same baryon fraction as actively star-forming, gas-dominated galaxies.

Indeed, there are examples of pairs of early- and late-type dwarfs that have indistinguishable baryonic masses and circular velocities, within the uncertainties. They occupy the same location in the bottom panel of Figure 4 despite their very different locations in the top panel. Examples of such matched pairs are given in Table 2. Each of these pairs has essentially the same baryon fraction m_b despite having very different stellar fractions m_*. Regardless of the physical reason for the observed behavior, baryonic mass is a more fundamental quantity than is the stellar mass alone, and a more reliable indicator of the dynamical mass.

5.2. Comparison with Stars and Gas in the EAGLE Simulations

In addition to establishing a kinematic relation analogous to abundance matching, we can also test the results of simulations that track baryons through their various phases. Evaluating all simulations is beyond the scope of this work, so as an example, we focus here on the EAGLE simulations (J. Schaye et al. 2015). P. D. Mitchell & J. Schaye (2022) quantified the variation of the mass in various baryonic components as a function of halo mass.

The accounting of P. D. Mitchell & J. Schaye (2022) includes stars, gas in the ISM, gas in the CGM, baryons that are ejected from their halos, and baryons that are prevented by feedback from accreting in the first place. The CGM dominates in massive halos ($M_{200} > 10^{13}\,M_\odot$), the vast majority of baryons are prevented from accreting onto low-mass halos ($M_{200} < 10^{11}\,M_\odot$), and the mass of ejected baryons dominates in between. At no point do stars dominate the simulated baryonic mass budget, and the gas of the ISM is always less than the stars. These latter are the components we measure directly.

The data and simulations are compared in Figure 6. The stellar mass follows the same qualitative trend in both. Quantitiatively, real galaxies have relatively more stars than anticipated at high mass. At intermediate masses, the situation is reversed, with fewer stars per unit dark matter. The scale in Figure 6 is logarithmic, so this is not a small difference, and the difference cannot be rectified with a variable f_v within the plausible range of that parameter. The EAGLE simulations do not probe low masses ($M_{200} < 10^{10}\,M_\odot$).

As noted by M. Korsaga et al. (2023), the gas mass-to-halo mass ratio is approximately constant in the data. This behavior is not seen in the simulations, where the fraction of cold gas in the ISM peaks around $M_{200} \sim 10^{12}\,M_\odot$, similar to the stars. Unlike the data, the gas mass fraction in the simulations declines rapidly to lower masses, and truncates abruptly at $M_{200} \sim 10^{10.5}\,M_\odot$. This scale corresponds to where most

[8] We define M_{200} to include all mass enclosed within r_{200} while many abundance matching relations refer to it as a parameter of the dark matter halo alone. The difference is small, so we make no attempt to reconcile it, as this encounters the subtle difficulty that an unknown fraction of the mass in the halo may be the local missing baryons.

[9] A. V. Kravtsov et al. (2018) adopted a definition that includes intracluster light as part of the central galaxy, which is one reason for its difference from the other abundance matching relations at high masses.

Table 2
Matched Pairs of Early- and Late-type Dwarfs

Pair	Type	Galaxy	M_*	M_g ($10^6\,M_\odot$)	M_b	V_f (km s^{-1})	References
1	ETG	NGC 185	140	…	140	48	(1)
	LTG	AGC 749237	53	77	130	49	(2)
2	ETG	Fornax	41	…	41	23	(1)
	LTG	AGC 111946	17	20	37	20	(2)
3	ETG	And VII	19	…	19	26	(1)
	LTG	AGC 112521	7	10	17	24	(2)
4	ETG	And XXXI	8.1	…	8.1	21	(1)
	LTG	AGC 748778	3.0	6.1	9.1	19	(2)
5	ETG	Sculptor	4.6	…	4.6	18	(1)
	LTG	DDO 210	0.7	2.7	3.4	16	(3)
6	ETG	Leo II	1.5	…	1.5	13	(1)
	LTG	Leo P	0.3	1.2	1.5	15	(4)
7	ETG	Tucana	1.1	…	1.1	12	(1)
	LTG	KK153	0.4	0.7	1.1	13	(5)

References. (1) S. S. McGaugh et al. (2021). (2) A. T. McNichols et al. (2016) (3) A. Begum et al. (2008). (4) E. Z. Bernstein-Cooper et al. (2014). (5) J.-L. Xu et al. (2025).

accretion is prevented by feedback in the EAGLE simulations (the dotted line in Figure 6). This suppression of cold gas in simulated low-mass objects is the opposite of what is seen in reality, as the majority of field galaxies are gas rich (with $M_g > M_*$; S. S. McGaugh et al. 2017). Very-low-mass, gas-rich galaxies exist, though it would seem that they should not (K. B. W. McQuinn et al. 2015). Feedback in the real Universe (F. Lelli et al. 2014; K. B. W. McQuinn et al. 2019; A. Marasco et al. 2023) appears to be less prolific at expelling or excluding baryons than the implementation of feedback in EAGLE.

We have restricted Figure 6 to the case of the EAGLE simulations (P. D. Mitchell & J. Schaye 2022) for clarity. Improvements in the simulation of gas physics as implemented in the successor simulations to EAGLE, COLIBRE (J. Schaye et al. 2025), might lead to a different answer, but a similar analysis to that of P. D. Mitchell & J. Schaye (2022) has not yet appeared as of this writing. On a related topic, COLIBRE produces disequilibrium rotation curves in dwarf galaxies (D. Dado et al. 2025) that are manifestly inconsistent with observational reality (R. Kuzio de Naray et al. 2009; R. Kuzio de Naray & T. Kaufmann 2011), so it is not possible to compare these simulated entities with observed galaxies that have well-measured V_f.

It is beyond the scope of this work to attempt an exhaustive exploration of all simulations. These differ in (i) the amount of mass that is expected in the CGM (R. J. Wright et al. 2024), (ii) that they anticipate more scatter than is observed (I. Medlock et al. 2025), and (ii) that they struggle with other aspects of gas in galaxies (A. Marasco et al. 2025). We thus return to what we can infer empirically from the data.

5.3. Missing Baryons

The obvious initial expectation was that the observed baryon content would trace the halo mass, so $m_b \sim$ constant (e.g., H. J. Mo et al. 1998). This is manifestly not the case in the data (Figure 4). Where do the local baryons currently reside? Why is the variation with mass so systematic?

Rich clusters of galaxies are the one type of system that meets the ideal $M_b \approx f_b M_{200}$. Averaging over the CLASH clusters analyzed by T. Mistele et al. (2025), we obtain $m_b = 0.154 \pm 0.038$, which is perfectly consistent with the cosmic baryon fraction ($f_b = 0.157$; Planck Collaboration et al. 2020). This ideal is not realized in lower-mass objects. The local baryon deficit is modest for groups and bright galaxies (J. N. Bregman et al. 2018; A. Dev et al. 2024; P. E. Mancera Piña et al. 2025; Y. Zhang et al. 2025b), and might plausibly be explained by the CGM. This is not the case for smaller masses. For every baryon that is detected in a galaxy with $M_b \approx 10^9\,M_\odot$, ∼10 baryons are missing. For dwarfs with $M_b \approx 10^7\,M_\odot$, ∼50 baryons are missing for every one that is observed (Figure 7).

To quantify the mass of missing baryons, we combine Equations (4) and (12) to obtain

$$\frac{M_X}{M_b} = \frac{1}{m_b} - 1 = \frac{1}{f_b \tanh\left(\frac{M_b}{M_0}\right)^{1/4}} - 1. \quad (13)$$

This ratio of missing-to-observed baryonic mass is plotted in Figure 7. Subtracting quantities and plotting the data as a linear ratio amplifies the appearance of the scatter. This is an artifact of error propagation; the source data themselves (the bottom panel of Figure 3) have remarkably little intrinsic scatter. The small intrinsic scatter around the expression for m_b in Equation (12) conveys to the ratio M_X/M_b in Equation (13): the mass in directly observed baryons M_b is eerily predictive of the expected mass in missing baryons M_X.

There are four possible solutions for the locally missing baryon problem: (i) they are present but not accounted for, (ii) they are absent, having been ejected or precluded from accreting in the first place, (iii) some systematic afflicts our mass estimates, or (iv) the ΛCDM paradigm is incorrect. In the

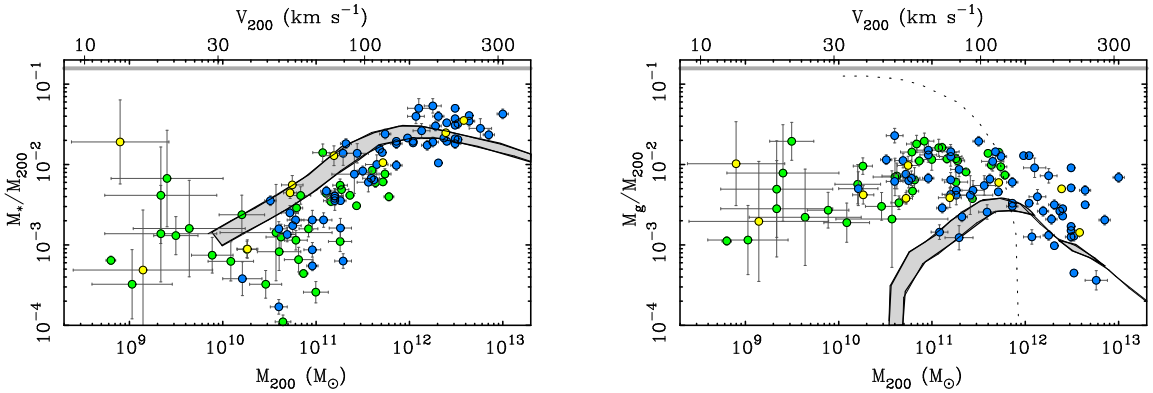

Figure 6. The stellar mass fraction (left panel) and gas mass fraction (right panel) as a function of mass M_{200} with the equivalent V_{200} on the top axis. Data and symbols are the same as in Figure 3; the sample is restricted to objects for which both stars and gas are directly measured for each galaxy. The lines show the expectation for central subhalos in the EAGLE simulations (P. D. Mitchell & J. Schaye 2022) with the width of the gray bands representing the range of f_v from 1 (bottom edge) to 1.4 (top edge). The dotted line in the right panel denotes the limit where gas is precluded from accreting onto halos in the EAGLE simulations.

first case, the unaccounted baryons may be lurking in the CGM of their parent dark matter halos (J. N. Bregman 2007; J. Tumlinson et al. 2017). In the second case, they would now reside in the IGM and not be associated with any particular galaxy. In the third, there may be something wrong with how we relate observed velocity to halo mass that leads us to infer missing baryons. Possibilities (i)–(iii) might all play a role, occurring in some fine-tuned combination. The fourth case admits the possibility that the problem arises because the necessary cosmic assumptions are incorrect. We discuss each of these possibilities in turn.

5.3.1. CGM

Perhaps the most obvious solution to the local missing baryon problem is for them not to be missing at all. There is no guarantee that all of the baryons in a halo cool and condense into the visible galaxy for which M_b is well measured. Some may remain mixed in with the dark matter halo out to (or even a bit beyond) the nominal virial radius, perhaps in the form of the warm-hot gas of the CGM (J. N. Bregman 2007; J. Tumlinson et al. 2017; J. N. Bregman et al. 2018).

Considerable progress has been made in detecting hot gas in the CGM of massive spiral galaxies (e.g., J. N. Bregman et al. 2022; Y. Zhang et al. 2024a). The uncertainties in the integrated masses are large, so it is unclear whether the CGM is enough to make up the observed shortfall. We illustrate the case of $M_X = M_{\rm CGM}$ in Figure 7 for three published measurements of Milky Way–mass galaxies: (1) the Milky Way coronal mass measurement of M. J. Miller & J. N. Bregman (2015), $M_{\rm CGM} = 4.3 \times 10^{10}\,M_\odot$, (2) the average of a dozen L^* galaxies by J. N. Bregman et al. (2022), $\langle M_{\rm CGM}\rangle = 9.8 \pm 2.8 \times 10^{10}\,M_\odot$, and (3) the fiducial estimate of the CGM mass of Milky Way analogs from Y. Zhang et al. (2025b), $M_{\rm CGM} = 1.26 \times 10^{11}\,M_\odot$. These would be sufficient to explain all of the missing baryons in the Milky Way if f_v were in the range 1.25–1.5. None suffice if $f_v = 1.0$, for which $M_X \approx 3.3 \times 10^{11}\,M_\odot$. The factor f_v thus plays a critical role in determining whether the local missing baryon problem appears to be solved by the CGM or not (see also S. S. McGaugh & P. van Dokkum 2021).

The need for missing baryons in massive galaxies (Figure 7) is greatly alleviated if $f_v \approx 1.4$. This eliminates the need entirely in some cases (P. E. Mancera Piña et al. 2025), but for most spiral galaxies with $M_b \approx 10^{11}\,M_\odot$, we infer $M_X \approx M_b$. That is, roughly as many baryons are missing as observed.

If there are as many baryons in the CGM as in the central galaxy itself, as seems plausible, then this might also explain the offset of our group measurements: the missing mass in groups might simply be the CGM of the galaxies that are members of the group. This interpretation seems satisfactory, but is not without issues. One is the offset between kinematic and lensing data that occurs when $f_v = 1.4$ is adopted (Figure 5). Another is that the equivalence of the CGM in groups and individual galaxies assumes $f_v = 1.0$ for the former but $f_v = 1.4$ for the latter. While this is possible in principle, there is no discontinuity in the data (Figure 3) before the notional factor f_v is introduced, so this would simply inject an artifact.

Much of the discussion has focused on bright galaxies with $M_b > 10^{10}\,M_\odot$. For lower-mass galaxies, $M_X = M_{\rm CGM} \approx M_b$ does not suffice to explain the local missing baryon problem. The amplitude of the problem is severe: galaxies with $M_b = 10^9\,M_\odot$ have $M_X \gtrsim 10\,M_b$. It gets worse to lower masses, sometimes reaching $M_X \approx 100\,M_b$ (Figure 7). It strains credulity to suppose that every dwarf galaxy hosts a CGM an order of magnitude more massive than itself, regardless of whether it is energetically possible (H. Katz et al. 2018).

5.3.2. IGM

Another possibility for the locally missing baryons is that they have been expelled from their host galaxies by feedback processes (J. Silk 2003), or precluded from accreting in the first place (P. D. Mitchell & J. Schaye 2022). In either case, the missing baryons we infer would reside in the IGM. L. Connor et al. (2025) estimated that the fraction of baryons in the IGM is $\sim 3/4$ while only $\sim 1/2$ of the dark matter is there. This is rather uncertain, but implies that some baryons have been expelled or excluded from galaxies. Moreover, some expulsion is required to account for the metallicity of the IGM (C. W. Danforth et al. 2006; E. Scannapieco et al. 2006).

The observed trend of decreasing baryon fraction with decreasing mass is suggestive of a role for binding energy: baryons may escape from smaller potential wells with increasing ease. This sounds plausible, but does not, by itself, provide an explanation for the particular trend that we observe. Supernova feedback is often invoked in this context, but the stochastic explosions of massive stars seem more likely to induce scatter than a smooth variation. Indeed, there is a great deal of scatter in some simulations (e.g., I. Medlock et al. 2025).

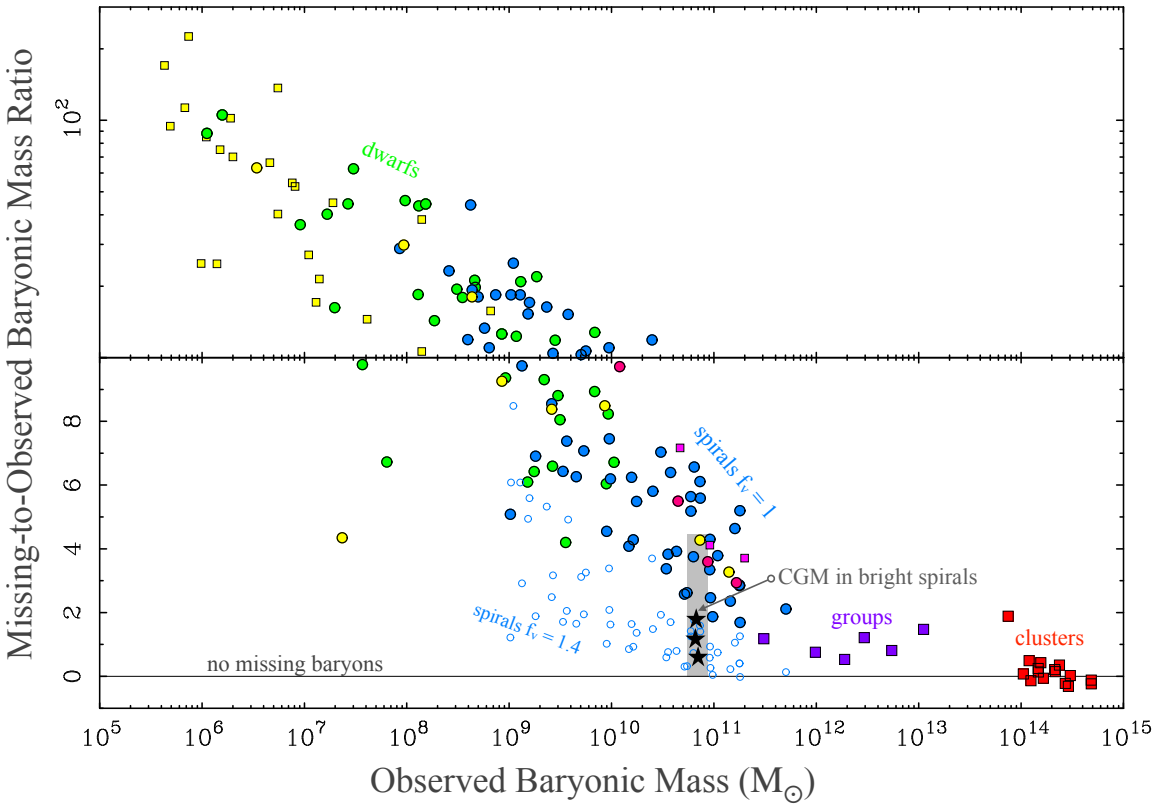

Figure 7. The ratio of missing-to-observed baryonic mass as a function of baryonic mass. Data and symbols are the same as in Figure 3. The ratio is linear in the bottom half of the diagram, then switches to logarithmic in the top half. Spiral galaxies of the WISE-SPARC sample are shown twice: once with $f_v = 1.0$ (solid blue circles) and again with $f_v = 1.4$ (small open circles). The Milky Way is the yellow point at the top of the gray band, which shows the range from zero CGM to that required to explain all of the locally missing baryons when $f_v = 1$. Stars represent the CGM measurements of Milky Way–mass galaxies by M. J. Miller & J. N. Bregman (2015), J. N. Bregman et al. (2022), and Y. Zhang et al. (2025b) from bottom to top.

In the EAGLE simulations (P. D. Mitchell & J. Schaye 2022), the majority of baryons are ejected from galaxy mass ($11 < M_{200} < 13\,M_\odot$) halos, but with little mass dependence: the depth of the potential wells is not the relevant effect.

Searches for evidence for feedback in dwarf galaxies have routinely obtained results (G. D. Bothun et al. 1994; F. Lelli et al. 2014; A. Concas et al. 2019) that contradict the expectation of vigorous outflows that could liberate the majority of baryons from their host halos (A. K. Leroy et al. 2015; K. B. W. McQuinn et al. 2019). To be sure there is some feedback, but rather than strong winds, there is more of a light breeze (A. Concas et al. 2017; A. Marasco et al. 2023) that does not suffice to unbind the entrained baryons and deliver them to the IGM (H. Katz et al. 2018). The same is observed at cosmic noon when star formation rates were much higher (A. Concas et al. 2022).

The mass dependence of the baryon deficit is very regular: $m_b \propto V_f \sim M_b^{1/4}$ with remarkably little scatter. This poses a fine-tuning problem. How do halos of the same mass always eject the same fraction of baryons?

It is, of course, possible to have the missing baryons reside in some combination of both the CGM and the IGM. However, invoking a combination of mechanisms exacerbates the amount of fine-tuning that is required. It does not suffice to say that some baryons remain in the CGM while others get ejected to in the IGM; we must also explain the variation with mass and the small scatter. D. Ruan et al. (2025) appeared to do this over a modest mass range, but their results are contingent on an abrupt change in the behavior of f_v around $\log M_b \sim 8.5$ (their Figure 7). This is not apparent in the data, which are smooth and continuous across this mass (Figure 3), so it appears that they have simply transferred the fine-tuning from one parameter (m_b) to another (f_v).

5.3.3. The Velocity Factor

So far, we have inferred variation in the baryon fraction assuming the observed rotation speed is a faithful indicator of the halo mass. Here, we consider whether variation in the velocity fraction f_v could avoid the inference of the local missing baryon problem.

For illustration, we fix $m_b = f_b$ so that only f_v varies. Rewriting Equations (9) and (10), inserting the adopted values of $\log A = 1.7$ and $\log B = 5.5$ and setting $m_b = f_b = 0.157$, we have

$$\log f_v = 1 - \frac{1}{3}\log V_f \tag{14}$$

$$= 1.14 - \frac{1}{12}\log M_b. \tag{15}$$

These hold for $5.7 < \log M_b < 13.68$. For $\log M_b \geqslant 13.68$, $f_v = 1$. Note that we could adopt a broken power law like this for Equations (11) and (12) or instead employ a hyperbolic tangent here as done there; lacking sufficient data to constrain the shape of the transition, either choice is valid at present.

In this fashion, it is mathematically possible to make the local baryon problem go away if and only if the velocity factor varies in the particular way given by Equation (15). This is

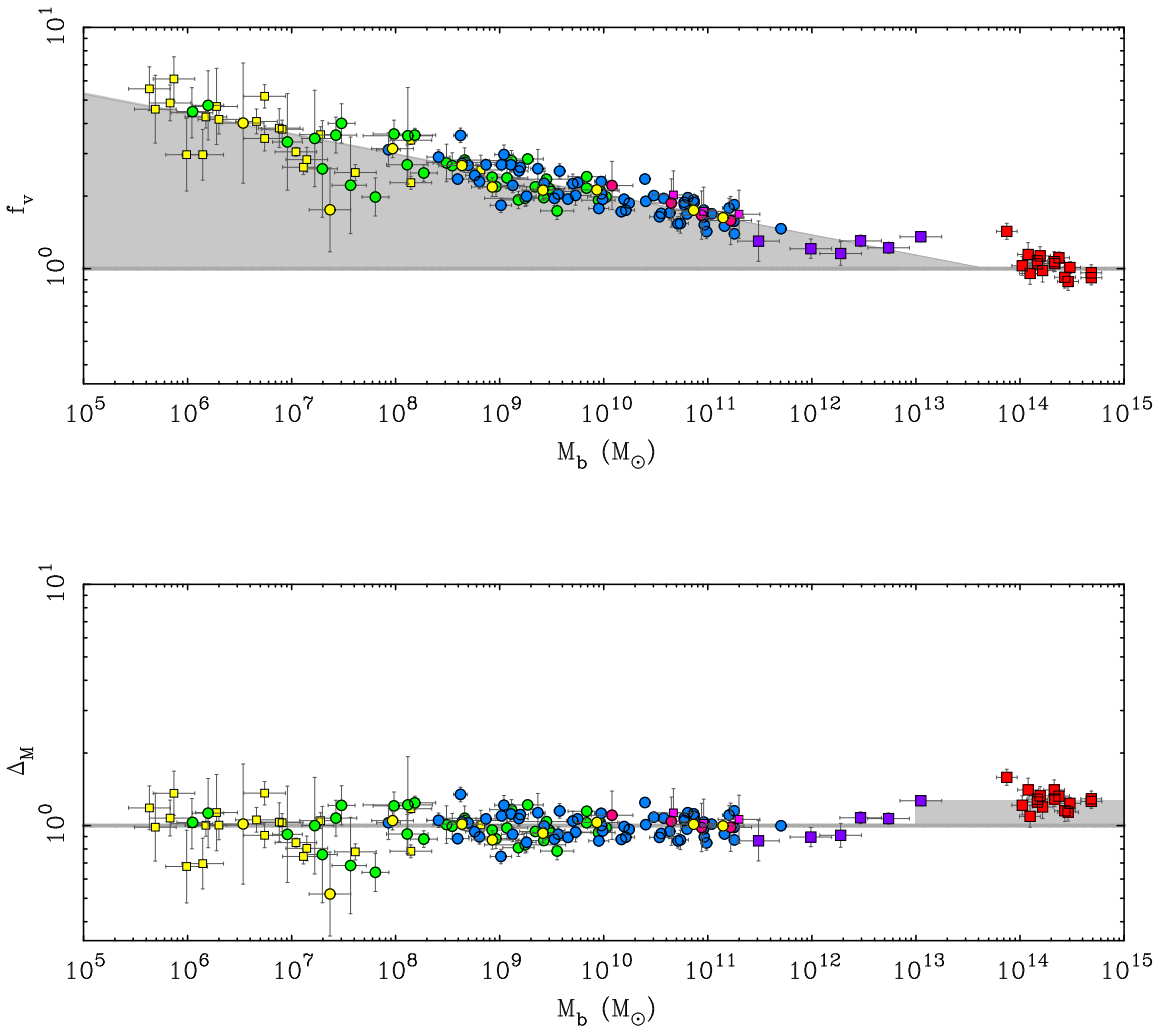

Figure 8. The velocity factor in ΛCDM (top panel) and the residual velocity in MOND (bottom panel) as a function of baryonic mass. Data and symbols as in Figure 3. The gray region illustrates where each theory gets it wrong. In ΛCDM, rich clusters of galaxies behave as expected, but explaining other systems requires $f_v \propto M_b^{-1/12}$ (Equation (15)). In MOND, we see the opposite effect: the observed baryons predict the correct velocity over the range $5 \times 10^5 \leqslant M_b < 10^{13}$ $M_\odot$, but falls short for larger masses, explaining only ∼80% of the velocity in clusters.

illustrated in Figure 8, which shows how f_v must increase as mass decreases. The gray region illustrates the deficit that we must attribute to missing baryons if f_v is constant.

Attributing all of the variation in the data to f_v is not viable (L. Posti et al. 2019). The magnitude of the required variation is too large, reaching $f_v \approx 4$ at low mass ($M_b \approx 3 \times 10^6\, M_\odot$). Such large values of f_v are inconsistent with rotation curve fits: $f_v < 2.4$ for all NFW fits (Figure 2), and it is usually much less. Worse, large f_v means that the observed velocity greatly exceeds that of the dark matter halo, contradicting the basic explanation of flat rotation curves. Some of the variation might be due to f_v, but it seems unlikely to be the dominant effect. Having both m_b and f_v vary implies a fine-tuning between them in order to maintain the smooth observed variation.

5.3.4. Paradigm Failure

The fourth possibility is that the local missing baryon problem arises because of a faulty assumption in the underlying paradigm. ΛCDM predicts a mass–velocity relation of the form $M_{200} \propto V_{200}^3$ (H. J. Mo et al. 1998; M. Steinmetz & J. F. Navarro 1999), while we observe something closer to $M_b \propto V_f^4$ (Figure 3). The inference that the fraction of missing baryons grows systematically greater with declining mass follows from the mismatch in slopes. This mismatch induces a curious result in the context of hierarchical galaxy assembly.

In the CDM cosmogony, small galaxies merge to form larger ones. Building large galaxies from small ones seems inconsistent with the observation that larger objects have higher baryon fractions. If baryons are ejected from small galaxies, they are not available to subsequently build larger galaxies. This incurs a teleological dilemma: a small halo needs to "know" if it will remain unmerged so that it should eject the "right" fraction of baryons for its mass or if it will later merge into a larger object so that it should retain the right amount to contribute to that higher baryon fraction object.

Ejection of baryons is not the only possible mechanism, but the concern holds regardless: there is a fine-tuning with mass that is not natural to hierarchical structure formation. Galaxies are the result of many mergers, so this puzzling fine-tuning occurs repeatedly, along every branch of every merger tree, each of which has many nodes. It is not obvious that a complex hierarchical merger history can lead to the uniform cold baryon fraction we observe at low redshift.

There is a disturbing reason underlying the mismatch in power-law slopes: the bulk of the data look like MOND (M. Milgrom 1983a). MOND is a modification of the force law suggested as an alternative to dark matter. It has had a remarkable number of a priori predictions corroborated by subsequent observations (S. S. McGaugh & W. J. G. de Blok 1998a; R. H. Sanders & S. S. McGaugh 2002; B. Famaey & S. S. McGaugh 2012), many of which were surprising (S. S. McGaugh & W. J. G. de Blok 1998b; I. Banik & H. Zhao 2022). These often lack a satisfactory explanation in terms of dark matter (S. McGaugh 2020). Strangely, the data do exactly as MOND predicts over seven decades in mass, $5.7 < \log(M_b/M_\odot) < 13$ (Figure 8).

There is no missing baryon problem in MOND for individual galaxies. What you see is what you get. This works so well that the masses of stars and gas within the confines[10] of the visible galaxy can be predicted by observing V_f, or vice versa (Figure 3). There is no dark matter model that performs so well (B. Famaey & S. S. McGaugh 2012).

The success of MOND persists for groups of galaxies analyzed via dynamics (M. Milgrom 2018, 2019) and for the groups of galaxies analyzed here via lensing, with the exception of the most-massive bin with $M_b \approx 10^{13}\,M_\odot$ (which is also an outlier in ΛCDM). It does not hold for groups with X-ray emission (G. W. Angus et al. 2008) or for rich clusters (R. H. Sanders 2003; P. Li et al. 2023; T. Mistele et al. 2025). For the highest-mass decade in Figure 8, $14 < \log M_b < 15$, MOND underpredicts the velocity: the observed baryons only explain 79% ± 7% of what is observed. Since $M_b \propto V_f^4$ in MOND, this offset in velocity is equivalent to a discrepancy of a factor of 2.3 in mass. This residual baryon discrepancy in MOND has been persistent (R. H. Sanders & S. S. McGaugh 2002; R. Kelleher & F. Lelli 2024), rather like the persistent absence of dark matter detections (J. Aalbers et al. 2025).

It is tempting to assert that MOND is falsified for its failure in clusters, and that may be correct (S. S. McGaugh 2024). However, it is hard to preclude the discovery of additional mass there, just as it is hard to preclude the existence of dark baryons in the halos of individual galaxies, as needed in ΛCDM. Both theories suffer a missing baryon problem; Figure 8 illustrates how they compare.

More disturbing philosophically is that the local missing baryon problem arises in ΛCDM *because* the data look like MOND. The baryon fraction in galaxies could have been pretty much anything less than the cosmic fraction. It could increase or decrease with mass, or not vary with mass at all, as we originally expected. The scatter from galaxy to galaxy could be huge, and arguably should be if driven by stochastic feedback processes (I. Medlock et al. 2025). In contrast, MOND predicts a unique behavior, and the data do exactly the one thing that MOND predicts over seven decades in mass. Why does so much of a ΛCDM Universe look like MOND?

6. Conclusions

We have combined kinematic and gravitational lensing data for galaxies and systems of galaxies to quantify the variation of the baryon fraction with mass. The data extend over a large dynamic range, from tiny dwarf galaxies to the largest clusters. We present novel gravitational lensing measurements for galaxy groups that help to inform the ill-constrained mass range between individual galaxies and rich clusters of galaxies.

We find a strong correlation between observed mass and the flat circular velocity V_f of the gravitational potential for objects with $V_f > 10\,\mathrm{km\,s^{-1}}$ (Figure 3). This is a Tully–Fisher–like relation that extends to galaxy groups and clusters of galaxies. The stellar mass M_*–V_f relation is strong for high-mass galaxies but exhibits scatter at low mass and a bifurcation between gas-rich and gas-poor galaxies (Figure 3). The baryonic (stars plus cold gas) mass M_b–V_f relation exhibits no bifurcation and little intrinsic scatter. Indeed, there are no second-parameter effects apparent in the M_b–V_f relation. In this respect, the observed baryonic mass of a galaxy is a more fundamental quantity than its stellar mass.

The data are well described by $M_b/M_{200} = f_b \tanh(M_b/M_0)^{1/4}$, where f_b is the cosmic baryon fraction and $M_0 \approx 5 \times 10^{13}\,M_\odot$ (Equation (12)). This kinematic mass matching relation provides a more precise estimator of dynamical mass than do stellar mass–halo mass relations obtained from abundance matching. There is some qualitative agreement between kinematic mass matching and abundance matching, but also significant quantitative tension between the two at both low and high mass (Figure 4).

The data imply a local missing baryon problem ($m_b < f_b$) for most systems. Rich clusters of galaxies are the exception, with $m_b = 0.154 \pm 0.038$, in good agreement with the cosmic baryon fraction, $f_b = 0.157$. Less-massive systems, from groups through giant galaxies to dwarfs, all have fewer detected baryons than the cosmic fraction. The amplitude of this discrepancy grows with decreasing mass. For galaxy groups and bright ($M_b \approx 10^{11}\,M_\odot$) galaxies, the discrepancy is modest (a factor of 2 or 3), so might plausibly be explained by the mass of gas in the CGM. However, the problem exceeds an order of magnitude for low-mass ($M_b \lesssim 10^9\,M_\odot$) galaxies where it strains credulity to imagine that >90% of the local missing baryons reside in the CGM while evading detection.

Galaxies with very different star formation histories have indistinguishable baryon fractions at the same mass (Table 2). This is not naturally explained by feedback that is driven by star formation for which one would expect a dependence on the current star formation rate or some time-integral over its variation. Simulations that include feedback have yet to successfully match the data (Figure 6). Indeed, the increase of baryon fraction with increasing mass seems contradictory to hierarchical galaxy formation, as merging low-mass galaxies with low baryon fractions would lead to larger galaxies with the same baryon fractions, not the higher baryon fractions that are observed. Fine-tuning thus seems unavoidable for ΛCDM models to simultaneously explain the observed variation of the baryon fraction with mass, its small intrinsic scatter, and its lack of dependence on star formation rate, gas fraction, or environment.

Where ΛCDM suffers a local missing baryon problem in galaxies, MOND suffers one in rich clusters with $M_b > 10^{13}\,M_\odot$ (Figure 8). However, the data over the range $5 \times 10^5 < M_b < 10^{13}\,M_\odot$ are more naturally explained by MOND. No tuning is necessary: a relation of this form was predicted a priori (M. Milgrom 1983b). We are not aware of a viable explanation for why so many of the predictions of MOND (B. Famaey & S. S. McGaugh 2012; I. Banik & H. Zhao 2022) are realized in a Universe made of dark matter.

[10] See Appendix B for a discussion of the CGM in MOND.

Acknowledgments

We thank the referee for providing comments that improved the presentation of these results. We are grateful to Joel Bregman for many detailed insights into the issues concerning the CGM. This work is based in part on observations made with ESO Telescopes at the La Silla Paranal Observatory under program IDs 177.A-3016, 177.A-3017, 177.A-3018, and 179.A-2004, and on data products produced by the KiDS consortium. The KiDS production team acknowledges support from: Deutsche Forschungsgemeinschaft, ERC, NOVA, and NWO-M grants; Target; the University of Padova, and the University Federico II (Naples). GAMA is a joint European-Australasian project based around a spectroscopic campaign using the Anglo-Australian Telescope. The GAMA input catalog is based on data taken from the Sloan Digital Sky Survey and the UKIRT Infrared Deep Sky Survey. Complementary imaging of the GAMA regions is being obtained by a number of independent survey programmes including GALEX MIS, VST KiDS, VISTA VIKING, WISE, Herschel-ATLAS, GMRT and ASKAP providing UV to radio coverage. GAMA is funded by the STFC (UK), the ARC (Australia), the AAO, and the participating institutions. The GAMA website is https://www.gama-survey.org/.

Appendix A
Groups

We consider groups from GAMA-II (S. P. Driver et al. 2011; J. Liske et al. 2015), specifically from version 10 of the "G3CFoFGroup" and "G3CGal" tables. Following D. Rana et al. (2022), S.-S. Li et al. (2024), Z. Liu et al. (2024), and M. Viola et al. (2015), we select groups with at least five members. We further enforce that the "BCG" of each group has a stellar mass estimate in the "StellarMassesLambdar" table. This leaves a total of 2751 groups. We split these into six bins by M_b, with bin edges $\log_{10} M_b/M_\odot = [11.0, 11.75, 12.2, 12.35, 12.6, 12.9, 13.3]$.

A.1. Baryonic and Stellar Masses

We assign a stellar and baryonic mass to each group using the following procedure. We start with the stellar masses of the member galaxies from the "StellarMassesLambdar" table version 24 (E. N. Taylor et al. 2011), applying the flux corrections listed in version 20 of that table, if these are not smaller than 1. Following T. Mistele et al. (2024a, 2024b), we correct the stellar masses of early-type galaxies by a factor of 1.4, where we define early-type galaxies as having $u - r > 2.2$ (I. Strateva et al. 2001), using the columns "fitflux_u" and "fitflux_r" of the "StellarMassesLambdar" table.

Following T. Mistele et al. (2024a, 2024b), we convert the stellar masses of the member galaxies into baryonic masses by adding gas according to two simple scaling relations. For early-types, we add a hot gas component (K.-H. Chae et al. 2020),

$$\frac{M_{g,\mathrm{hot}}}{M_*} = 10^{-5.414} \cdot \left(\frac{M_*}{M_\odot}\right)^{0.47}. \tag{A1}$$

For late-type galaxies, we add a cold gas component (F. Lelli et al. 2016c; S. S. McGaugh et al. 2020)

$$\frac{M_{g,\mathrm{cold}}}{M_*} = \frac{1}{X}\left(11550\left(\frac{M_*}{M_\odot}\right)^{-0.46} + 0.07\right), \tag{A2}$$

where

$$X = 0.75 - 38.2\left(\frac{M_*}{1.5 \cdot 10^{24} M_\odot}\right)^{0.22}. \tag{A3}$$

The first term in Equation (A2) represents atomic gas, and the second term takes into account molecular gas. Equation (A3) accounts for the variation of the hydrogen fraction X as metallicity varies with stellar mass (S. S. McGaugh et al. 2020).

A few member galaxies do not have a stellar mass listed in "StellarMassesLambdar." For simplicity, we set their stellar and baryonic masses to zero. This occurs in only a handful of cases when many hundreds of groups inform each mass bin, so the effect on our results is negligible.

We then sum up the members' stellar masses to obtain the stellar mass of the groups. We apply the flux correction from A. S. G. Robotham et al. (2011) for $N_{\mathrm{FoF}} \geqslant 5$. This is only a small correction in the lower M_b bins (due to the relatively small redshift), but becomes a factor of a few in the highest M_b bin (due to the higher redshift). We follow the same procedure to assign baryonic masses to the groups. Strictly speaking, the flux correction factor from A. S. G. Robotham et al. (2011) does not apply directly to the baryonic masses, but we expect that it gives at least a first reasonable approximation.

A.2. V_f from Weak Lensing

We use weak gravitational lensing observations to measure stacked mass profiles $M(r)$ of the galaxy groups and infer a flat circular velocity V_f from these.

A.2.1. Excess Surface Density

We first use ellipticities from the KiDS-1000 SOM-gold source galaxy catalog (K. Kuijken et al. 2019; A. H. Wright et al. 2020; B. Giblin et al. 2021; H. Hildebrandt et al. 2021) to measure the so-called excess surface density $\Delta\Sigma$ around each group, i.e., around each lens l,

$$\Delta\Sigma_l(R) = \frac{1}{1+\mu}\frac{\sum_s W_{ls}\Sigma_{\mathrm{crit},ls}\epsilon_{t,ls}}{\sum_s W_{ls}}. \tag{A4}$$

Here, the W_{ls} are weights, $\epsilon_{t,ls}$ denotes the tangential ellipticity of the source s with respect to the lens l, $\Sigma_{\mathrm{crit},ls}$ is the critical surface density, and $1 + \mu$ corrects for multiplicative biases. The sums run over all source galaxies s within a given radial bin around the group. The critical surface density is calculated following M. M. Brouwer et al. (2021) and A. Dvornik et al. (2017) and takes into account uncertainties in the source redshifts,

$$\Sigma^{-1}_{\mathrm{crit},ls} = \frac{4\pi G_{\mathrm{N}}}{c^2} D(z_l) \int_{z_l}^{\infty} dz_s\, n_{ls}(z_s) \cdot \frac{D(z_l, z_s)}{D(z_s)}. \tag{A5}$$

The function $n_{ls}(z)$ is determined as follows. For a given z_l and a given photometric source redshift $z_{B,s}$, we check in which of the five tomographic bins from H. Hildebrandt et al. (2021) the $z_{B,s}$ value belongs, get the corresponding redshift distribution function from H. Hildebrandt et al. (2021), and normalize this distribution to unity in the interval $[z_l, \infty)$. The weights W_{ls} are given by $W_{ls} = w_s \Sigma^{-2}_{\mathrm{crit},ls}$ where w_s estimates the precision of

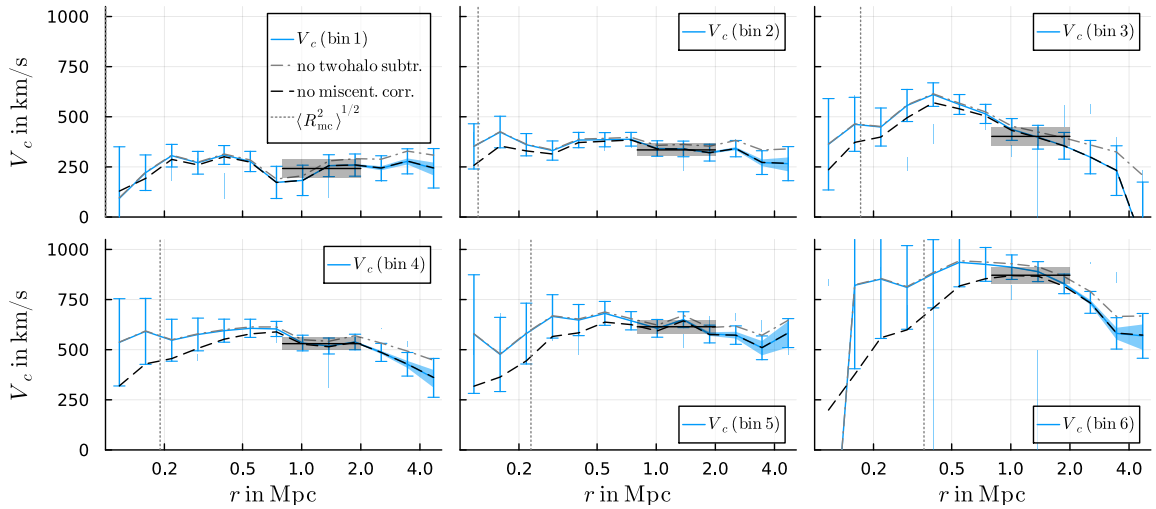

Figure 9. The stacked mass profiles $M(r)$ of the GAMA groups in each bin in terms of the implied circular velocity $V_c(r) = \sqrt{GM(r)/r}$ (solid blue lines). The blue band indicates the systematic uncertainty from extrapolating $\Delta\Sigma_l$ beyond the last measured data point (Appendix A.2.2). Error bars indicate the statistical uncertainties. Dashed vertical lines indicate the estimated miscentering offsets $\sqrt{\langle R_{\rm mc}^2 \rangle}$ that we correct for. Dashed black lines indicate the V_c we obtain without this miscentering correction. The miscentering correction is valid only at radii significantly larger than the miscentering offset (Appendix A.2.3). Dashed–dotted gray lines indicate the V_c we obtain without subtracting the two-halo term (Appendix A.2.6). Miscentering is important at small radii, and the two-halo term is important at large radii. The shaded black region indicates V_f, its statistical uncertainty, and the radial range from which it is calculated.

the ellipticity measurement of the source s (M. M. Brouwer et al. 2021; B. Giblin et al. 2021). We adopt $1 + \mu = 0.98531$ from M. M. Brouwer et al. (2021). We use 13 logarithmic radial bins, with the smallest bin edge being 0.1 Mpc and with a logarithmic bin width of $1/7.5$.

A.2.2. Mass Profile

We convert the excess surface density $\Delta\Sigma_l(R)$ into a mass profile $M_l(r)$ using the nonparametric method from T. Mistele et al. (2024a, 2024b) and T. Mistele & A. Durakovic (2024), which is based on the following deprojection formula:

$$M_l(r) = 4r^2 \int_0^{\pi/2} d\theta \; \Delta\Sigma_l\left(\frac{r}{\sin\theta}\right). \tag{A6}$$

To evaluate this integral, we must know $\Delta\Sigma_l(R)$ at all radii, up to $R = \infty$. In practice, we measure $\Delta\Sigma_l(R)$ only up to a finite maximum radius $R_{\rm max}$ and only in discrete radial bins, so we need to both interpolate and extrapolate $\Delta\Sigma_l$. We interpolate linearly and extrapolate assuming that $\Delta\Sigma_l$ is proportional to $1/R$ beyond $R_{\rm max}$.

As discussed in T. Mistele et al. (2024a, 2024b), the precise choices of how to interpolate and extrapolate are relatively unimportant over the bulk of the radial range and become important only close to $R_{\rm max}$. This is illustrated by the blue band in Figure 9, which shows the range of masses obtained by making the opposite and extreme choices of extrapolating $\Delta\Sigma_l$ assuming its decay is proportional to $1/R^2$ (as fast as for a point mass) and $1/\sqrt{R}$ (slower than for a singular isothermal sphere). The extrapolation is unimportant in the radial range we use for V_f (see below).

A.2.3. Miscentering

In practice, the coordinates of the group centers are not known very accurately. We adopt the luminosity-weighted center of mass ("CenRA" and "CenDEC" in "G3CFoFGroup"), but this does not necessarily reflect the true center of the gravitational potential. As a result, $\Delta\Sigma_l(R)$, and therefore $M_l(r)$, are often underestimated at small radii. T. Mistele & A. Durakovic (2024) derived a formula that allows one to approximately and statistically correct for miscentering, given that one knows the average miscentering offset. The formula applies at radii larger than the miscentering offset and corresponds to replacing $\Delta\Sigma_l(R)$ by[11]

$$\Delta\Sigma_l(R) + \frac{1}{4}\frac{\langle R_{\rm mc}^2 \rangle}{R^2}\Delta_{\rm mc}(R), \tag{A7}$$

where $R_{\rm mc}$ is the miscentering offset and

$$\Delta_{\rm mc}(R) \equiv (4 - R\partial_R - R^2\partial_R^2)\Delta\Sigma_l(R). \tag{A8}$$

Since we linearly interpolate the observed $\Delta\Sigma_l$ (see Appendix A.2.2), the second-order derivative in Equation (A8) is not well defined. However, this second-order derivative is ultimately integrated over in Equation (A6) so that we can use integration by parts to get rid of it. Indeed, instead of replacing $\Delta\Sigma_l$ with Equation (A7), we can keep $\Delta\Sigma_l$ as is and replace Equation (A6) with the following deprojection formula:

$$M_l(r) = 4r^2 \int_0^{\pi/2} d\theta \left(\Delta\Sigma_l\left(\frac{r}{\sin\theta}\right) + \frac{1}{4}\frac{\langle R_{\rm mc}^2 \rangle}{r^2}(I_1 + I_2 + I_3)\right), \tag{A9}$$

where

$$\begin{aligned} I_1 &= 4s_\theta^2 \, \Delta\Sigma_l\left(\frac{r}{s_\theta}\right), \\ I_2 &= -(t_\theta^2 + 2s_\theta^2)\left(\Delta\Sigma_l\left(\frac{r}{s_\theta}\right) - \Delta\Sigma_l(r)\right), \\ I_3 &= -\left(s_\theta + \frac{t_\theta}{c_\theta}\right)\left(r\Delta\Sigma_l'\left(\frac{r}{s_\theta}\right) - r\Delta\Sigma_l'(r)\right). \end{aligned} \tag{A10}$$

[11] We assume that the convergence κ is negligible for groups, so that we can replace G_+ by $\Delta\Sigma$ in the formulas from T. Mistele & A. Durakovic (2024).

Here, a prime denotes a derivative of $\Delta\Sigma_l$ with respect to its argument, and we used the shorthand notation $s_\theta = \sin\theta$, $c_\theta = \cos\theta$, and $t_\theta = \tan\theta$. Importantly, there are no longer any second-order derivatives so that we can apply this formula to our linearly interpolated $\Delta\Sigma_l$.

As discussed in Appendix A.2.2, in practice, we extrapolate $\Delta\Sigma_l$ beyond the last data point at $R_{\rm max}$. To implement that, we split the integral in Equation (A6) at $\theta = \arcsin(r/R_{\rm max})$. This leads to boundary terms when integrating by parts, resulting in a slightly longer version of Equation (A10) that we give in Appendix A.2.9.

We adopt the following simple estimate of $\langle R_{\rm mc}^2\rangle$. We assume that the differences between the three different group center coordinates provided by GAMA are representative of the true miscentering offset. The three different coordinates correspond to the luminosity-weighted center, the BCG, and the so-called iterative center. For each group, we calculate the three pairwise offsets between these three different centers, square the mean, and then average across all groups within a given M_b bin. This simple procedure produces $\langle R_{\rm mc}^2\rangle$ estimates that are roughly consistent with those implied by the best-fit results from D. Rana et al. (2022). It also reproduces the trend of higher-mass bins having larger miscentering offsets.

Our procedure is illustrated in Figure 9 (solid blue versus dashed black lines). Miscentering effects are generally small at radii much larger than $\sqrt{\langle R_{\rm mc}^2\rangle}$ (vertical dashed gray lines in Figure 9), but become significant at smaller radii. For our main results below, we consider only radii where miscentering is likely only a small effect, i.e., radii larger than a few times $\sqrt{\langle R_{\rm mc}^2\rangle}$.

Our miscentering correction formulas originate in a Taylor expansion in $(R_{\rm mc}/r)^2$ (T. Mistele & A. Durakovic 2024) and are therefore only valid at radii significantly larger than $R_{\rm mc}$. At smaller radii, these formulas tend to over-correct $M(r)$. This is another reason to consider only radii larger than a few times $\sqrt{\langle R_{\rm mc}^2\rangle}$.

A.2.4. Stacking

We stack the mass profiles $M_l(r)$ of all groups in a given M_b bin,

$$M(r) \equiv \frac{\sum_l w_l(r) M_l(r)}{\sum_l w_l(r)}, \tag{A11}$$

with weights $w_l(r)$ given by the inverse square of the uncertainty on $M_l(r)$

$$w_l(r) \equiv \frac{1}{\sigma^2_{M_l(r)}\,|_{\rm from\ \epsilon_t}}. \tag{A12}$$

Specifically, for w_l we consider only the uncertainty induced by the ellipticities $\epsilon_{t,ls}$, not additional uncertainties in, for example, $\langle R_{\rm mc}^2\rangle$ (see Appendix A.2.8). This is to not hinder the intrinsic ellipticities of the source galaxies from canceling out.

We use the same weights to calculate averaged stellar and baryonic masses in each bin. Following T. Mistele et al. (2024a), we adopt $\langle\sqrt{M_b}\rangle^2$ as the averaged baryonic mass and similarly for the averaged stellar mass.

A.2.5. Additive Biases

To take into account additive biases, we use the procedure described above to measure the mass profiles around 1 million random points in each of the three GAMA regions G09, G12, and G15. We use the pre-defined random coordinates from the GAMA table "Randoms" version 2. This results in three stacked profiles $M_{{\rm random},i}(r)$ where i labels the three regions. For each group, we subtract the $M_{{\rm random},i}(r)$ of the corresponding region from that group's $M_l(r)$ in Equation (A11).

A.2.6. Two-halo Term

The procedure described above assumes that the observed lensing signal is entirely due to the galaxy groups themselves. At large radii, however, contributions from the groups' local environments become important. We follow the procedure from T. Mistele et al. (2025) to subtract this so-called two-halo term. This procedure is based on the following estimate of the contribution of the two-halo term to the excess surface density $\Delta\Sigma$ (e.g., J. Guzik & U. Seljak 2001; M. Oguri & T. Hamana 2011; G. Covone et al. 2014):

$$\Delta\Sigma_{\rm 2h}(R) = b\frac{\bar\rho_{m,0}}{2\pi D(z_l)^2}\int_0^\infty d\ell\ \ell \times J_2\left(\frac{\ell R}{D(z_l)}\right)P_m(k_\ell; z_l). \tag{A13}$$

Here, J_2 denotes the second Bessel function of the first kind, b is the bias according to J. L. Tinker et al. (2010), $\bar\rho_{m,0}$ is the mean matter density at redshift $z = 0$, and $P_m(k_\ell;z_l)$ is the linear matter power spectrum at $k_\ell = \ell/[(1+z)D(z_l)]$. We compute the contribution of $\Delta\Sigma_{\rm 2h}$ to our inferred mass $M(r)$ and subtract it (see T. Mistele et al. 2025 for details). The bias factor b depends on the halo mass M_{200} of the lens under consideration. For the purpose of calculating $\Delta\Sigma_{\rm 2h}$, we treat each M_b bin as a single lens located at the mean redshift of the bin and with the stacked $M(r)$ as its mass profile.

This simple procedure does not allow for a quantitatively precise subtraction of the two-halo term. It does, however, serve as a rough first estimate of its size and of the affected radii. For our main results below, we consider only radii small enough for the two-halo term to have only a minor effect. This is illustrated in Figure 9 (solid blue lines versus dashed–dotted gray lines).

A.2.7. Flat Circular Velocities

We convert the stacked $M(r)$ into a stacked circular velocity via $V_c(r)^2 \equiv GM(r)/r$. We take V_f to be the weighted average of the circular velocities in the radial bins between 800 kpc and 2 Mpc, with weights given by the inverse squared uncertainty of V_c. This radial range is chosen to be larger than typical miscentering offsets (Appendix A.2.3) but small enough for the two-halo term to have only a moderate effect (Appendix A.2.6).

The flat rotation speed obtained in this way is illustrated by the shaded region in Figure 9. Most bins have a range of nearly constant rotation speed, but bin 3 declines steadily, and bin 6 truncates with unphysical abruptness. The group data look more ragged than that for stacked individual galaxies (T. Mistele et al. 2024a), which we attribute largely to the difference in the number of available systems: there are hundreds of groups per bin but thousands of galaxies. The

group mass range is also difficult to probe free of external effects, so we see no reason to infer a different behavior from the indefinite flatness seen in both lower- and higher-mass systems.

A.2.8. Statistical Uncertainties

We take into account the statistical uncertainties σ_ϵ in the source galaxy ellipticities (B. Giblin et al. 2021) and the uncertainty $\sigma_{\langle R_{\rm mc}^2\rangle}$ in $\langle R_{\rm mc}^2\rangle$. We adopt $\sigma_{\langle R_{\rm mc}^2\rangle} = \langle R_{\rm mc}^2\rangle$, corresponding to a Rayleigh distribution (D. E. Johnston et al. 2007).

We propagate these uncertainties into the final result using linear error propagation. To this end, we first use analytical formulas to calculate the covariance matrix $\mathrm{Cov}(M(r), M(r'))$ for the stacked mass profile before applying the two-halo subtraction. These analytical formulas are conceptually similar to those given in Appendix A of T. Mistele et al. (2024a), but additionally correct for miscentering and take into account that a given source s can contribute to multiple groups (see also M. Viola et al. 2015). These analytical formulas are given in Appendix A.2.9. In a second step, we propagate this covariance matrix of the un-subtracted mass profile into a covariance matrix for the two-halo subtracted mass profile using automatic differentiation (T. Mistele & A. Durakovic 2024; T. Mistele et al. 2025).

A.2.9. Analytical Formulas for Mass Profiles and Covariance Matrices

For each individual group, before stacking, we use the following deprojection formula, which explicitly shows how we correct for miscentering and how we extrapolate $\Delta\Sigma_l(R)$ beyond $R_{\rm max}$:

$$\begin{aligned} &M_l(r)\cdot(4r^2)^{-1} \\ &= \int_{\theta_0}^{\pi/2} d\theta \left(\Delta\Sigma_l\left(\frac{r}{\sin\theta}\right) + \frac{1}{4}\frac{R_{\rm mc}^2}{r^2}(I_1+I_2+I_3)\right) \\ &-\frac{1}{4}\left(\frac{R_{\rm mc}}{r}\right)^2 \sin^2\theta_0\tan\theta_0\left(\Delta\Sigma_l\left(\frac{r}{\sin\theta_0}\right) - \Delta\Sigma_l(r)\right) \\ &-\frac{1}{4}\left(\frac{R_{\rm mc}}{r}\right)^2 \sin\theta_0\tan\theta_0\left(r\Delta\Sigma_l'\left(\frac{r}{\sin\theta_0}\right) - r\Delta\Sigma_l'(r)\right) \\ &+\int_0^{\theta_0} d\theta \Delta\Sigma_l^{\rm powerlaw}\left(\frac{r}{\sin\theta}\right), \end{aligned} \tag{A14}$$

where $\theta_0 \equiv \arcsin(r/R_{\rm max})$, and $\Delta\Sigma_l^{\rm powerlaw}(R)$ is the extrapolation of $\Delta\Sigma_l(R)$ beyond $R_{\rm max}$. We assume a simple power law $1/R^{n_{\rm extrap}}$, which, at $R = R_{\rm max}$, is matched to the miscentering-corrected observed $\Delta\Sigma_l$. The integrands I_1, I_2, I_3 are defined in Appendix A.2.3.

We now list the analytical formulas that we use to numerically evaluate Equation (A14) and the covariance matrix of the resulting stacked mass profiles. Let $R_1, R_2, \ldots, R_N \equiv R_{\rm max}$ be the discrete radii where we measure $\Delta\Sigma_l$, in increasing order. Since Equation (A14) is linear in $\Delta\Sigma_l$ and since we linearly interpolate between the discrete measured $\Delta\Sigma_l$ data points, Equation (A14) is of the form

$$M_l(R_\alpha) = 4R_\alpha^2 \sum_{i=\alpha}^{N} C_{\alpha i}\Delta\Sigma_l(R_i), \tag{A15}$$

for some coefficients C that are independent of the $\Delta\Sigma$ measurements ($\alpha = 1, \ldots, N$). As we will see below, they are of the form $C_{\alpha i} = C_{\alpha i}^{(0)} + R_{\rm mc}^2 C_{\alpha i}^{(1)}$ where $C^{(0)}$ and $C^{(1)}$ are independent of $R_{\rm mc}^2$. That is, the coefficients C are linear in $R_{\rm mc}^2$.

The covariance matrix for the stacked masses $M(r)$ from Equation (A11) can then be written as

$$\begin{aligned} \mathrm{Cov}(M(R_\alpha), M(R_\beta)) = \sum_s \sigma_{\epsilon_s}^2 (&X_{\alpha s}[\sin]X_{\beta s}[\sin] \\ &+ X_{\alpha s}[\cos]X_{\beta s}[\cos]) + \sigma_{R_{\rm mc}^2}^2 Y_\alpha Y_\beta, \end{aligned} \tag{A16}$$

where σ_{ϵ_s} is the ellipticity dispersion of the source s from Table 1 of B. Giblin et al. (2021) and

$$\begin{aligned} X_{\alpha s}[f] \equiv \sum_l \sum_{i=\alpha}^{N} \Big|_{R_{ls}=R_i} &4R_\alpha^2 w_l(R_\alpha)\langle C_{\alpha i}\rangle Z_{li}^{-1} W_{ls} \\ &\times \Sigma_{{\rm crit},ls} f(2\phi_{\rm ls}), \end{aligned} \tag{A17}$$

$$Y_\alpha \equiv \sum_l \sum_{i=\alpha}^{N} 4R_\alpha^2 w_l(R_\alpha)\langle \Delta\Sigma_\alpha(R_i)\rangle \frac{\partial C_{\alpha i}}{\partial R_{\rm mc}^2}, \tag{A18}$$

where the "$R_{ls} = R_i$" indicates that the sum is restricted to lenses l relative to which the source s is located in the ith radial bin. Further, ϕ_{ls} is the position angle of the source with respect to the lens, $Z_{li} \equiv \sum_s|_{R_{ls}=R_i} W_{ls}$, and $\partial C_{\alpha i}/\partial R_{\rm mc}^2 \equiv C_{\alpha i}^{(1)}$. For the expectation value $\langle C_{\alpha i}\rangle$, we use $C_{\alpha i}$ with $R_{\rm mc}^2$ replaced by $\langle R_{\rm mc}^2\rangle$, and for the expectation value $\langle\Delta\Sigma_l(R_i)\rangle$, we use the point estimate Equation (A4). This formula is conceptually similar to the analytical covariance matrix from M. Viola et al. (2015) and follows from linear error propagation assuming that $R_{\rm mc}^2$ is independent of the source ellipticities ϵ.

It remains to give the definition of the coefficients C. We adopt the following shorthand notations:

$$\begin{aligned} &x_{\alpha i} \equiv \frac{R_\alpha}{R_i},\ \theta_{\alpha i} \equiv \arcsin(x_{\alpha i}), \\ &\Delta\theta_{\alpha i} \equiv \theta_{\alpha i} - \theta_{\alpha,i+1},\ c_{\alpha i} \equiv \sqrt{1-x_{\alpha i}^2}. \end{aligned} \tag{A19}$$

We can decompose $C_{\alpha i}$ into three parts corresponding to their respective origin in Equation (A14),

$$C_{\alpha i} = C_{\alpha i}^{\rm bulk} + C_{\alpha i}^{\rm boundary} + C_{\alpha i}^{\rm tail}. \tag{A20}$$

We start with $C_{\alpha i}^{\rm bulk}$, which we further decompose as

$$C_{\alpha i}^{\rm bulk} = a_{\alpha i} + b_{\alpha,i-1} + \delta_{i\alpha}A_\alpha + \delta_{i,\alpha+1}B_\alpha, , \tag{A21}$$

where δ is the Kronecker delta, and the coefficients $a_{\alpha i}$, $b_{\alpha,i-1}$, A_α, B_α, are identically zero for $\alpha = N$. Further, $a_{\alpha N} = 0$ and

$b_{\alpha,\alpha-1} = 0$. For $\alpha < N$, we have

$$B_\alpha \equiv \frac{R_{\rm mc}^2}{4R_\alpha^2}\left[\frac{x_{\alpha,\alpha+1}(x_{\alpha,\alpha+1}-1)-1}{\sqrt{\frac{1}{x_{\alpha,\alpha+1}^2}-1}} + \frac{x_{\alpha,\alpha+1}}{1-x_{\alpha,\alpha+1}}\left(\frac{x_{\alpha,\alpha+1}^2}{c_{\alpha,\alpha+1}} - \frac{x_{\alpha,N}^2}{c_{\alpha N}}\right)\right],$$
$$A_\alpha \equiv -B_\alpha + \frac{R_{\rm mc}^2}{4R_\alpha^2}\left(\frac{x_{\alpha,\alpha+1}^3}{c_{\alpha,\alpha+1}} - \frac{x_{\alpha,N}^3}{c_{\alpha N}}\right). \quad \text{(A22)}$$

Further, we have for $\alpha < N$ and $i \geqslant \alpha$,

$$a_{\alpha i} = \frac{a_{\alpha i}^{(0)} + a_{\alpha i}^{(1)} + a_{\alpha i}^{(2)} + a_{\alpha i}^{(3)}}{x_{\alpha,i+1} - x_{\alpha i}},$$
$$b_{\alpha i} = \frac{b_{\alpha i}^{(0)} + b_{\alpha i}^{(1)} + b_{\alpha i}^{(2)} + b_{\alpha i}^{(3)}}{x_{\alpha,i+1} - x_{\alpha i}}, \quad \text{(A23)}$$

with

$$a_{\alpha i}^{(0)} \equiv -x_{\alpha i}\Delta\theta_{\alpha i} + x_{\alpha i}x_{\alpha,i+1}(\text{arctanh}(c_{\alpha,i+1}) - \text{arctanh}(c_{\alpha i})),$$
$$-b_{\alpha i}^{(0)} \equiv -x_{\alpha,i+1}\Delta\theta_{\alpha i} + x_{\alpha i}x_{\alpha,i+1}(\text{arctanh}(c_{\alpha,i+1}) - \text{arctanh}(c_{\alpha i})),$$
$$a_{\alpha i}^{(1)} \equiv \frac{R_{\rm mc}^2}{4R_\alpha^2}[x_{\alpha i}x_{\alpha,i+1}(2c_{\alpha,i+1} - 4c_{\alpha i}) - 2x_{\alpha i}\Delta\theta_{\alpha i} + x_{\alpha i}\sin(2\theta_{\alpha i})],$$
$$-b_{\alpha i}^{(1)} \equiv \frac{R_{\rm mc}^2}{4R_\alpha^2}[x_{\alpha i}x_{\alpha,i+1}(4c_{\alpha,i+1} - 4c_{\alpha i}) - 2x_{\alpha,i+1}\Delta\theta_{\alpha i} + x_{\alpha,i+1}(\sin(2\theta_{\alpha i}) - \sin(2\theta_{\alpha,i+1}))],$$
$$a_{\alpha i}^{(2)} \equiv \frac{R_{\rm mc}^2}{4R_\alpha^2}\cdot\begin{cases}\frac{x_{\alpha i}x_{\alpha,i+1}}{c_{\alpha i}}\left(1 - c_{\alpha i}c_{\alpha,i+1} + x_{\alpha i}^2\left(\frac{x_{\alpha i}}{x_{\alpha,i+1}} - 2\right)\right), & \alpha \neq i,\\ 0, & \alpha = i,\end{cases}$$
$$-b_{\alpha i}^{(2)} \equiv -a_{\alpha i}^{(2)}\,|_{i\leftrightarrow i+1},$$
$$a_{\alpha i}^{(3)} \equiv \frac{R_{\rm mc}^2}{4R_\alpha^2}\cdot\begin{cases}x_{\alpha i}x_{\alpha,i+1}\left(\frac{x_{\alpha,i+1}^2}{c_{\alpha,i+1}} - \frac{x_{\alpha i}^2}{c_{\alpha i}}\right), & \alpha \neq i,\\ 0, & \alpha = i,\end{cases}$$
$$-b_{\alpha i}^{(3)} \equiv a_{\alpha i}^{(3)}. \quad \text{(A24)}$$

The "$i \leftrightarrow i+1$" next to $a_{\alpha i}^{(2)}$ indicates to first take the expression for $a_{\alpha i}^{(2)}$ and then swap all i and $i+1$ indices in that expression. For $C_{\alpha i}^{\rm boundary}$, we have $C_{Ni}^{\rm boundary} = 0$ and, for $\alpha < N$,

$$C_{\alpha i}^{\rm boundary} = -\frac{1}{4}\left(\frac{R_{\rm mc}}{R_\alpha}\right)^2 \sin^2\theta_{\alpha N}\tan\theta_{\alpha N}(\delta_{iN} - \delta_{i\alpha}) - \frac{1}{4}\left(\frac{R_{\rm mc}}{R_\alpha}\right)^2 \sin\theta_{\alpha N}\tan\theta_{\alpha N}R_\alpha \times\left(\frac{\delta_{iN} - \delta_{i,N-1}}{R_N - R_{N-1}} - \frac{\delta_{i,\alpha+1} - \delta_{i\alpha}}{R_{\alpha+1} - R_\alpha}\right). \quad \text{(A25)}$$

Finally, $C_{\alpha i}^{\rm tail}$ is given by

$$C_{\alpha i}^{\rm tail} = \delta_{iN}\frac{1 - c_{\alpha N}}{x_{\alpha N}}\left(1 + \frac{1}{4}\left(\frac{R_{\rm mc}}{R_N}\right)^2(4 - n_{\rm extrap}^2)\right). \quad \text{(A26)}$$

Appendix B
The Role of the CGM in MOND

ΛCDM and MOND are such different theories that it can be difficult to compare their predictions, even with the same data. The visible galaxy composed of stars and cold gas (H I and H_2) is the same in both cases. In ΛCDM, it is natural to consider the CGM that is within the virial radius of the dark matter halo to be part of each galaxy. There is no dark matter in MOND, so this concept is meaningless: there is no dark matter halo (Figure 1) with an artificial boundary at r_{200} or any other overdensity. Any gas in the vicinity of a galaxy but beyond its apparent limits is merely circumgalactic: in the same neighborhood, but not necessarily distinct from the IGM. There is no expectation for its mass or radial extent and no baryon budget for it to aspirationally fill.

In MOND, the observed baryons $M_b = M_* + M_g$ in the central galaxy are the appropriate quantity to compare to the measured flat rotation speed V_f that encloses them. There is no need for an intermediary factor f_v to relate V_f to some notional halo quantity at larger radius. However, there is a subtle geometric effect as we transition from the edge of the disk where the kinematic V_f is measured to much larger radii where gravitational lensing provides an estimate of V_f (T. Mistele et al. 2024a).

MOND predicts an absolute relation between mass and flat rotation speed (M. Milgrom 1983a):

$$a_0 G M_b = V_f^4. \quad \text{(B1)}$$

This is the origin of the empirical BTFR in MOND, but strictly applies at very large radii where the gravitational potential is effectively spherical. Since a flattened mass rotates faster than the equivalent spherical distribution (J. Binney & S. Tremaine 1987), the intercept A of the BTFR (Equation (8)) is related to the acceleration scale a_0 of MOND by the factor ζ such that

$$A = \frac{\zeta}{a_0 G}. \quad \text{(B2)}$$

The geometric factor $\zeta = 1$ for spheres but is slighlty different for other mass distributions. A razor-thin exponential disk has $\zeta \approx 0.76$ at four scale lengths (S. S. McGaugh & W. J. G. de Blok 1998a), typical of where V_f is measured. We can infer the effective value of ζ for finite thickness disks by fitting the

BTFR: $A = 50\,M_\odot\,\mathrm{km}^{-4}\,\mathrm{s}^4$ when $(a_0 G)^{-1} = 63\,M_\odot\,\mathrm{km}^{-4}\,\mathrm{s}^4$ (S. S. McGaugh 2005), so $\zeta \approx 0.8$. The exact value of ζ can vary with the individual thickness of each galaxy, but this effect is too subtle to detect at present.

For the kinematic data, V_f is measured where $\zeta \approx 0.8$ is appropriate. As we probe to much larger radii with gravitational lensing, all galaxies begin to resemble point masses, so we expect $\zeta \to 1$. If there were no mass in the CGM, this should result in slowly declining rotation curves and an offset between the kinematic and lensing BTFR. No such offset is observed (T. Mistele et al. 2024a), though the uncertainties may preclude its notice (T. Mistele et al. 2024b).

In principle, this provides yet another test of MOND. In practice, it depends on the mass in the CGM. For a rotation curve to remain exactly flat from tens to hundreds of kiloparsecs implies additional mass to counterbalance the transition in ζ such that $M_b \to \zeta^{-1} M_b$. This extra velocity would be accounted for if $M_{\rm CGM} \approx 0.25\,M_b$.

There already exists a similar effect in the transition from stars to atomic gas. By itself, an exponential stellar disk in MOND predicts a slight dip in rotation speed in the outskirts of galaxies (M. Milgrom 1983b) that is not observed (S. M. Kent 1987). This is an artifact of neglecting the atomic gas, which has a more extended mass distribution (M. Milgrom 1988).

Rotation curves need not be exactly flat; their shapes depend on the mass distribution (M. Milgrom 1983b). This is not well measured for the CGM, but to provide an example, S. S. McGaugh (2018) built models of the Milky Way both with and without a CGM component. For the CGM component, the mass distribution suggested by M. J. Miller & J. N. Bregman (2015; $M_{\rm CGM} = 4.3 \times 10^{10}\,M_\odot$ out to 250 kpc) was adopted ($M_{\rm CGM} \approx 0.6\,M_b$). This increases the MOND-predicted velocity from $V(R = 100\,\mathrm{kpc}) = 190\,\mathrm{km\,s^{-1}}$ without any CGM to $196\,\mathrm{km\,s^{-1}}$ with it, so the effect is subtle. In the case of the Milky Way, it may be impossible to accurately measure the circular velocity of the potential at such large radii due to the perturbation of the LMC (R. Brada & M. Milgrom 2000; G. Besla et al. 2007; W. Oehm & P. Kroupa 2024).

The effect of the CGM on the extended rotation curves of galaxies in MOND depends on each individual mass distribution, but in general, additional mass would increase V_f (Equation (B1)). However, the presence of other galaxies also matters. Rotation curves cannot remain flat to infinity; at some point, the influence of other objects comes to dominate. This external field effect causes the rotation velocity at very large radii to decline (K.-H. Chae et al. 2020), acting in the opposite sense of additional mass in any CGM. These offsetting effects can be difficult to disentangle (K.-H. Chae et al. 2021).

ORCID iDs

Stacy S. McGaugh https://orcid.org/0000-0002-9762-0980
Tobias Mistele https://orcid.org/0000-0001-7048-3173
Francis Duey https://orcid.org/0009-0003-1662-5179
Konstantin Haubner https://orcid.org/0009-0007-7808-4653
Federico Lelli https://orcid.org/0000-0002-9024-9883
James M. Schombert https://orcid.org/0000-0003-2022-1911
Pengfei Li https://orcid.org/0000-0002-6707-2581

References

Aalbers, J., Akerib, D. S., Musalhi, A. K. A., et al. 2025, PhRvL, 135, 011802
Andreon, S., Wang, J., Trinchieri, G., Moretti, A., & Serra, A. L. 2017, A&A, 606, A24
Angus, G. W., Famaey, B., & Buote, D. A. 2008, MNRAS, 387, 1470
Banik, I., & Zhao, H. 2022, Symm, 14, 1331
Begum, A., Chengalur, J. N., Karachentsev, I. D., Sharina, M. E., & Kaisin, S. S. 2008, MNRAS, 386, 1667
Behroozi, P. S., Wechsler, R. H., & Conroy, C. 2013, ApJL, 762, L31
Bernstein-Cooper, E. Z., Cannon, J. M., Elson, E. C., et al. 2014, AJ, 148, 35
Besla, G., Kallivayalil, N., Hernquist, L., et al. 2007, ApJ, 668, 949
Bilicki, M., Dvornik, A., Hoekstra, H., et al. 2021, A&A, 653, A82
Binney, J., & Tremaine, S. 1987, Galactic Dynamics (Princeton Univ. Press)
Bothun, G. D., Eriksen, J., & Schombert, J. M. 1994, AJ, 108, 913
Brada, R., & Milgrom, M. 2000, ApJL, 531, L21
Bregman, J. N. 2007, ARA&A, 45, 221
Bregman, J. N., Anderson, M. E., Miller, M. J., et al. 2018, ApJ, 862, 3
Bregman, J. N., Hodges-Kluck, E., Qu, Z., et al. 2022, ApJ, 928, 14
Brouwer, M. M., Oman, K. A., Valentijn, E. A., et al. 2021, A&A, 650, A113
Bullock, J. S., & Boylan-Kolchin, M. 2017, ARA&A, 55, 343
Chae, K.-H., Desmond, H., Lelli, F., McGaugh, S. S., & Schombert, J. M. 2021, ApJ, 921, 104
Chae, K.-H., Lelli, F., Desmond, H., et al. 2020, ApJ, 904, 51
Concas, A., Maiolino, R., Curti, M., et al. 2022, MNRAS, 513, 2535
Concas, A., Popesso, P., Brusa, M., Mainieri, V., & Thomas, D. 2019, A&A, 622, A188
Concas, A., Popesso, P., Brusa, M., et al. 2017, A&A, 606, A36
Connor, L., Ravi, V., Sharma, K., et al. 2025, NatAs, 9, 1226
Copi, C. J., Schramm, D. N., & Turner, M. S. 1995, Sci, 267, 192
Covone, G., Sereno, M., Kilbinger, M., & Cardone, V. F. 2014, ApJL, 784, L25
Crain, R. A., Eke, V. R., Frenk, C. S., et al. 2007, MNRAS, 377, 41
Dado, D., Oman, K. A., Harborne, K. E., et al. 2026, MNRAS, 547, stag356
Danforth, C. W., Shull, J. M., Rosenberg, J. L., & Stocke, J. T. 2006, ApJ, 640, 716
de Blok, W. J. G., & McGaugh, S. S. 1997, MNRAS, 290, 533
de Blok, W. J. G., McGaugh, S. S., Bosma, A., & Rubin, V. C. 2001, ApJL, 552, L23
Dev, A., Driver, S. P., Meyer, M., et al. 2024, MNRAS, 535, 2357
Di Cintio, A., Brook, C. B., Dutton, A. A., et al. 2014a, MNRAS, 441, 2986
Di Cintio, A., Brook, C. B., Macciò, A. V., et al. 2014b, MNRAS, 437, 415
Draine, B. T. 2011, Physics of the Interstellar and Intergalactic Medium (Princeton Univ. Press)
Driver, S. P., Hill, D. T., Kelvin, L. S., et al. 2011, MNRAS, 413, 971
Duey, F., Schombert, J., McGaugh, S., & Lelli, F. 2024, AJ, 168, 19
Duey, F., Schombert, J., McGaugh, S., & Lelli, F. 2025, AJ, 169, 186
Duffy, A. R., Schaye, J., Kay, S. T., et al. 2010, MNRAS, 405, 2161
Dvornik, A., Cacciato, M., Kuijken, K., et al. 2017, MNRAS, 468, 3251
Famaey, B., & McGaugh, S. S. 2012, LRR, 15, 10
Famaey, B., Pizzuti, L., & Saltas, I. D. 2025, PhRvD, 111, 123042
Fukugita, M., Hogan, C. J., & Peebles, P. J. E. 1998, ApJ, 503, 518
Giblin, B., Heymans, C., Asgari, M., et al. 2021, A&A, 645, A105
Giovanelli, R., Haynes, M. P., Adams, E. A. K., et al. 2013, AJ, 146, 15
Gnedin, O. Y., Kravtsov, A. V., Klypin, A. A., & Nagai, D. 2004, ApJ, 616, 16
Gonzalez, A. H., Sivanandam, S., Zabludoff, A. I., & Zaritsky, D. 2013, ApJ, 778, 14
Governato, F., Zolotov, A., Pontzen, A., et al. 2012, MNRAS, 422, 1231
Guzik, J., & Seljak, U. 2001, MNRAS, 321, 439
Haubner, K., Lelli, F., Di Teodoro, E., et al. 2025, A&A, 696, A185
Hildebrandt, H., van den Busch, J. L., Wright, A. H., et al. 2021, A&A, 647, A124
Hoeft, M., & Gottloeber, S. 2010, AdAst, 2010, 693968
Hua, Z., Lelli, F., Di Teodoro, E., McGaugh, S., & Schombert, J. 2025, A&A, 703, A223
Iorio, G., Fraternali, F., Nipoti, C., et al. 2017, MNRAS, 466, 4159
Johnston, D. E., Sheldon, E. S., Tasitsiomi, A., et al. 2007, ApJ, 656, 27
Katz, H., Desmond, H., Lelli, F., et al. 2018, MNRAS, 480, 4287
Katz, H., Desmond, H., McGaugh, S., & Lelli, F. 2019, MNRAS, 483, L98
Katz, H., Lelli, F., McGaugh, S. S., et al. 2017, MNRAS, 466, 1648
Kelleher, R., & Lelli, F. 2024, A&A, 688, A78
Kent, S. M. 1987, AJ, 93, 816
Kormendy, J., & Freeman, K. C. 2016, ApJ, 817, 84
Korsaga, M., Famaey, B., Freundlich, J., et al. 2023, ApJL, 952, L41
Kravtsov, A. V., Vikhlinin, A. A., & Meshcheryakov, A. V. 2018, AstL, 44, 8
Kuijken, K., Heymans, C., Dvornik, A., et al. 2019, A&A, 625, A2

Kuzio de Naray, R., & Kaufmann, T. 2011, MNRAS, 414, 3617
Kuzio de Naray, R., McGaugh, S. S., & Mihos, J. C. 2009, ApJ, 692, 1321
Laganá, T. F., Martinet, N., Durret, F., et al. 2013, A&A, 555, A66
Lelli, F., McGaugh, S. S., & Schombert, J. M. 2016a, AJ, 152, 157
Lelli, F., McGaugh, S. S., & Schombert, J. M. 2016b, ApJL, 816, L14
Lelli, F., McGaugh, S. S., & Schombert, J. M. 2016c, AJ, 152, 157
Lelli, F., McGaugh, S. S., Schombert, J. M., Desmond, H., & Katz, H. 2019, MNRAS, 484, 3267
Lelli, F., McGaugh, S. S., Schombert, J. M., & Pawlowski, M. S. 2017, ApJ, 836, 152
Lelli, F., Verheijen, M., & Fraternali, F. 2014, A&A, 566, A71
Leroy, A. K., Walter, F., Martini, P., et al. 2015, ApJ, 814, 83
Li, J.-T., Bregman, J. N., Wang, Q. D., Crain, R. A., & Anderson, M. E. 2018, ApJL, 855, L24
Li, P., Lelli, F., McGaugh, S., & Schombert, J. 2020, ApJS, 247, 31
Li, P., McGaugh, S. S., Lelli, F., Schombert, J. M., & Pawlowski, M. S. 2022a, A&A, 665, A143
Li, P., McGaugh, S. S., Lelli, F., et al. 2022b, ApJ, 927, 198
Li, P., Tian, Y., Júlio, M. P., et al. 2023, A&A, 677, A24
Li, S.-S., Hoekstra, H., Kuijken, K., Schaller, M., & Schaye, J. 2025, A&A, 700, A202
Liske, J., Baldry, I. K., Driver, S. P., et al. 2015, MNRAS, 452, 2087
Liu, Z., Xu, K., Zhang, J., Wang, W., & Liu, C. 2025, ApJ, 987, 4
Mancera Piña, P. E., Read, J. I., Kim, S., et al. 2025, A&A, 699, A311
Marasco, A., Belfiore, F., Cresci, G., et al. 2023, A&A, 670, A92
Marasco, A., de Blok, W. J. G., Maccagni, F. M., et al. 2025, A&A, 697, A86
McGaugh, S. 2020, Galax, 8, 35
McGaugh, S. S. 2005, ApJ, 632, 859
McGaugh, S. S. 2011, PhRvL, 106, 121303
McGaugh, S. S. 2012, AJ, 143, 40
McGaugh, S. S. 2018, RNAAS, 2, 156
McGaugh, S. S. 2024, Clusters of Galaxies Ruin Everything https://tritonstation.com/2024/02/06/clusters-of-galaxies-ruin-everything/
McGaugh, S. S., & de Blok, W. J. G. 1998a, ApJ, 499, 66
McGaugh, S. S., & de Blok, W. J. G. 1998b, ApJ, 499, 41
McGaugh, S. S., de Blok, W. J. G., Schombert, J. M., Kuzio de Naray, R., & Kim, J. H. 2007, ApJ, 659, 149
McGaugh, S. S., Lelli, F., & Schombert, J. M. 2020, RNAAS, 4, 45
McGaugh, S. S., Lelli, F., Schombert, J. M., et al. 2021, AJ, 162, 202
McGaugh, S. S., & Schombert, J. M. 2014, AJ, 148, 77
McGaugh, S. S., & Schombert, J. M. 2015, ApJ, 802, 18
McGaugh, S. S., Schombert, J. M., Bothun, G. D., & de Blok, W. J. G. 2000, ApJL, 533, L99
McGaugh, S. S., Schombert, J. M., de Blok, W. J. G., & Zagursky, M. J. 2010, ApJL, 708, L14
McGaugh, S. S., Schombert, J. M., & Lelli, F. 2017, ApJ, 851, 22
McGaugh, S. S., & van Dokkum, P. 2021, RNAAS, 5, 23
McGaugh, S. S., & Wolf, J. 2010, ApJ, 722, 248
McNichols, A. T., Teich, Y. G., Nims, E., et al. 2016, ApJ, 832, 89
McQuinn, K. B. W., Adams, E. A. K., Cannon, J. M., et al. 2022, ApJ, 940, 8
McQuinn, K. B. W., Skillman, E. D., Dolphin, A., et al. 2015, ApJ, 812, 158
McQuinn, K. B. W., van Zee, L., & Skillman, E. D. 2019, ApJ, 886, 74
Medlock, I., Neufeld, C., Nagai, D., et al. 2025, ApJ, 980, 61
Milgrom, M. 1983a, ApJ, 270, 365
Milgrom, M. 1983b, ApJ, 270, 371
Milgrom, M. 1988, ApJ, 333, 689
Milgrom, M. 2018, PhRvD, 98, 104036
Milgrom, M. 2019, PhRvD, 99, 044041
Miller, M. J., & Bregman, J. N. 2015, ApJ, 800, 14
Mistele, T., & Durakovic, A. 2024, OJAp, 7, 120
Mistele, T., Lelli, F., McGaugh, S., Schombert, J., & Famaey, B. 2025, OJAp, 8, 132
Mistele, T., McGaugh, S., Lelli, F., Schombert, J., & Li, P. 2024a, ApJL, 969, L3
Mistele, T., McGaugh, S., Lelli, F., Schombert, J., & Li, P. 2024b, JCAP, 2024, 020
Mitchell, P. D., & Schaye, J. 2022, MNRAS, 511, 2600
Mo, H. J., Mao, S., & White, S. D. M. 1998, MNRAS, 295, 319
Moster, B. P., Naab, T., & White, S. D. M. 2013, MNRAS, 428, 3121
Muñoz-Cuartas, J. C., Macciò, A. V., Gottlöber, S., & Dutton, A. A. 2011, MNRAS, 411, 584
Namumba, B., Ianjamasimanana, R., Koribalski, B., et al. 2025, A&A, 699, A372
Navarro, J. F., Frenk, C. S., & White, S. D. M. 1997, ApJ, 490, 493
Oñorbe, J., Boylan-Kolchin, M., Bullock, J. S., et al. 2015, MNRAS, 454, 2092
Oehm, W., & Kroupa, P. 2024, Univ, 10, 143
Oguri, M., & Hamana, T. 2011, MNRAS, 414, 1851
Peebles, P. J. E. 1984, ApJ, 277, 470
Planck Collaboration, Aghanim, N., Akrami, Y., et al. 2020, A&A, 641, A6
Posti, L., Marasco, A., Fraternali, F., & Famaey, B. 2019, A&A, 629, A59
Pratt, C. T., Qu, Z., & Bregman, J. N. 2021, ApJ, 920, 104
Rana, D., More, S., Miyatake, H., et al. 2022, MNRAS, 510, 5408
Riess, A. G., Yuan, W., Macri, L. M., et al. 2022, ApJL, 934, L7
Robotham, A. S. G., Norberg, P., Driver, S. P., et al. 2011, MNRAS, 416, 2640
Ruan, D., Brooks, A. M., Cruz, A., et al. 2025, MNRAS, 541, 2180
Sanders, R. H. 2003, MNRAS, 342, 901
Sanders, R. H., & McGaugh, S. S. 2002, ARA&A, 40, 263
Scannapieco, E., Pichon, C., Aracil, B., et al. 2006, MNRAS, 365, 615
Schaye, J., Crain, R. A., Bower, R. G., et al. 2015, MNRAS, 446, 521
Schaye, J., Chaikin, E., Schaller, M., et al. 2025, arXiv:2508.21126
Schombert, J., McGaugh, S., & Lelli, F. 2019, MNRAS, 483, 1496
Schombert, J., McGaugh, S., & Lelli, F. 2020, AJ, 160, 71
Schombert, J., McGaugh, S., & Lelli, F. 2022, AJ, 163, 154
Sellwood, J. A., & McGaugh, S. S. 2005, ApJ, 634, 70
Shull, J. M., Smith, B. D., & Danforth, C. W. 2012, ApJ, 759, 23
Silk, J. 2003, MNRAS, 343, 249
Simon, J. D. 2019, ARA&A, 57, 375
Skordis, C., & Złośnik, T. 2021, PhRvL, 127, 161302
Stark, D. V., McGaugh, S. S., & Swaters, R. A. 2009, AJ, 138, 392
Steigman, G., & Turner, M. S. 1985, NuPhB, 253, 375
Steinmetz, M., & Navarro, J. F. 1999, ApJ, 513, 555
Strateva, I., Ivezić, Ž., Knapp, G. R., et al. 2001, AJ, 122, 1861
Taylor, E. N., Hopkins, A. M., Baldry, I. K., et al. 2011, MNRAS, 418, 1587
Tinker, J. L., Robertson, B. E., Kravtsov, A. V., et al. 2010, ApJ, 724, 878
Trachternach, C., de Blok, W. J. G., McGaugh, S. S., van der Hulst, J. M., & Dettmar, R. 2009, A&A, 505, 577
Tully, R. B., & Fisher, J. R. 1977, A&A, 54, 661
Tully, R. B., Rizzi, L., Shaya, E. J., et al. 2009, AJ, 138, 323
Tumlinson, J., Peeples, M. S., & Werk, J. K. 2017, ARA&A, 55, 389
van Albada, T. S., Bahcall, J. N., Begeman, K., & Sancisi, R. 1985, ApJ, 295, 305
Viola, M., Cacciato, M., Brouwer, M., et al. 2015, MNRAS, 452, 3529
Walker, T. P., Steigman, G., Kang, H.-S., Schramm, D. M., & Olive, K. A. 1991, ApJ, 376, 51
Walter, F., Brinks, E., de Blok, W. J. G., et al. 2008, AJ, 136, 2563
Wright, A. H., Hildebrandt, H., van den Busch, J. L., & Heymans, C. 2020, A&A, 637, A100
Wright, R. J., Somerville, R. S., Lagos, C. d. P., et al. 2024, MNRAS, 532, 3417
Xu, J.-L., Zhu, M., Yu, N.-P., et al. 2025, ApJL, 982, L36
Zhang, Y., Comparat, J., Ponti, G., et al. 2024a, A&A, 690, A267
Zhang, Y., Comparat, J., Ponti, G., et al. 2024b, A&A, 690, A268
Zhang, Y., Comparat, J., Ponti, G., et al. 2025, A&A, 693, A197
Zhang, Y., Shreeram, S., Ponti, G., et al. 2026, A&A, 706, A102